

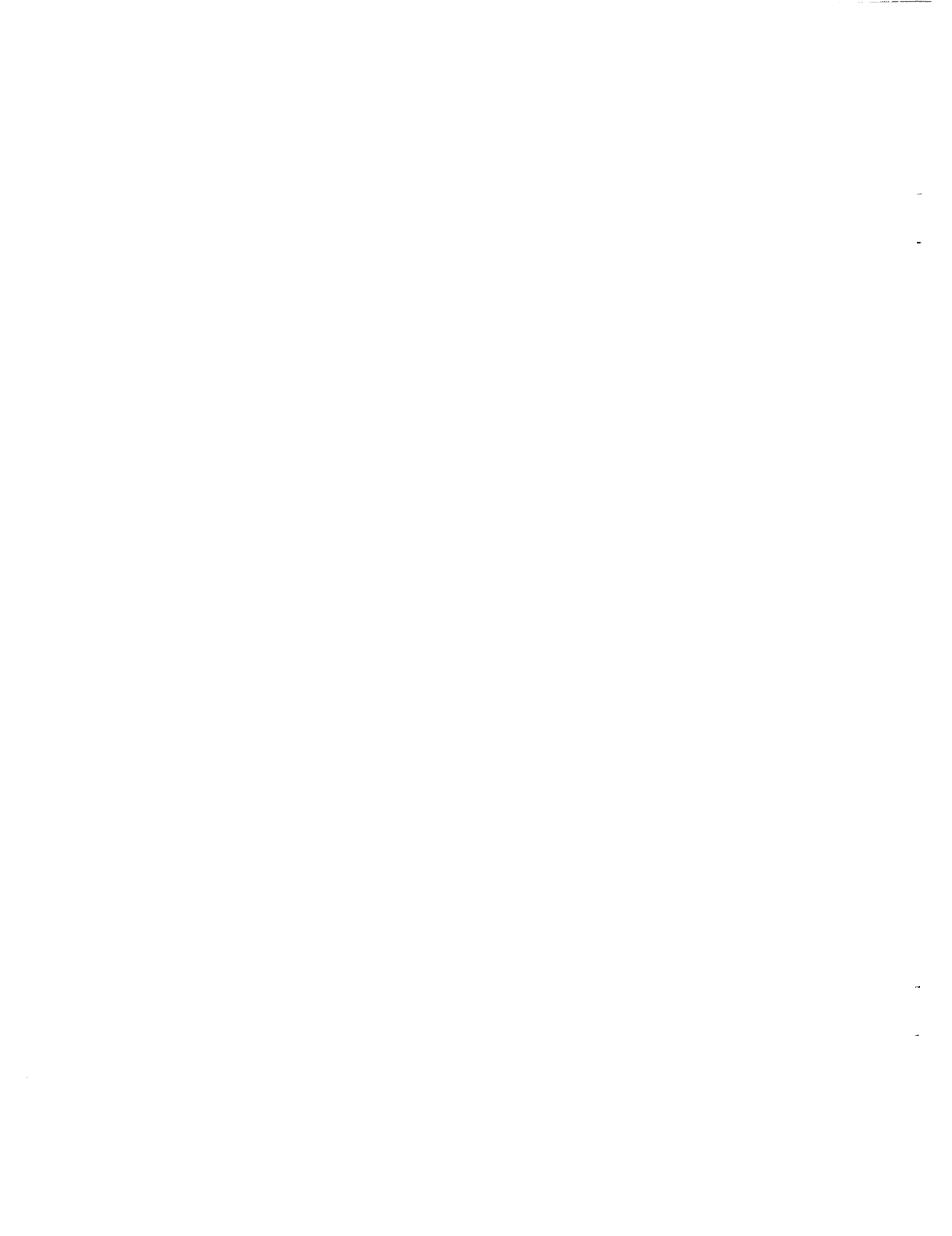
NASA CR-189109

Development of an Improved Mirror Facet for Space Applications

**Paul Schertz, P.E., Shabbar Salfie,
and Luke Lammert**

October 1991

**Prepared for
National Aeronautics and Space Administration
Lewis Research Center
Cleveland, Ohio 44135
Under Contract NAS3-25632**



Contents

	Page
Summary	1
1.0 Introduction	3
2.0 Specifications and Material Selection	5
2.1 Specifications	5
2.1.1 Slope Error	5
2.1.2 Specular Reflectance	6
2.1.3 Other Specifications	7
2.2 Material Selection	7
3.0 Thermal and Distortion Analysis	13
4.0 Adhesive Selection and Testing	17
4.1 Initial Market Survey	17
4.2 Initial Evaluation	18
4.3 Extended Adhesive Evaluations	18
4.3.1 Humidity Cycling	20
4.3.2 Temperature Cycling	20
4.3.3 Ultrasonic Test Results	21
4.3.4 Microscopic Inspection	21
5.0 Coatings	23
6.0 Sheet Forming	29
7.0 Facet Fabrication	31
7.1 Preparation of Surfaces for Facet Fabrication	31
7.2 Facet Fabrication Procedures	33
7.2.1 The Panel Fabrication Work Area	33
7.2.2 Placing the Facet Sheet on the Mold	34
7.2.3 Transferring Adhesive to the Core and Core Transfer to the Mold	35
7.2.4 Placing the Back Sheet	35
7.2.5 Mounting Tooling Alignment	36
7.2.6 Edge Trimming/Sealing	36
7.2.7 Mounting the Support Hardware	37
8.0 Measurement of Facet Slope Error	39
8.1 Measurement of 300 mm Spherical Facet Slope Error	39
8.2 Measurement of Full-Size Facet Slope Errors	40
9.0 Discussion of Results	47
10.0 Summary of Results	49
Appendix A Computer Program for Facet Contour Data Reduction	51
References	69
Report Documentation Page	100

List of Tables

Table	Title	Page
2.1	Metal Candidates and Properties	71
3.1	Material Properties of Thermal Analysis	72
5.1	Properties of Levelling and Reflective Coats	73
8.1	Sensitivity of Measured Local Slope Error to Direction of Scan	73

List of Figures

Figure	Description	Page
1.1	Facet Configuration	74
2.1	Relative Sensitivity to Slope Error	75
2.2	Calculated Reflectance Spectra Averaged over AMO for Al as a Function of Al ₂ O ₃ Overcoat Thickness	75
2.3	Reflectance of Specular Aluminum	76
2.4	Reflectance of Levelized Aluminums	76
2.5	Soldered Facet Sample	77
3.1	Incident Radiation on Front Face of Concentrator	78
3.2	Orbit Geometry for the Collector	78
3.3	Finite Element Model of Unit Cell	79
3.4	Transient Temperature Response of the Facet	80
3.5	Contour Plot of Facet Displacement at Low Temperature	81
3.6	Contour Plot of Facet Displacement at High Temperature	82
4.1	Ultrasonic Results of Early Facet Sample	83
4.2	Ultrasonic Results of Later Facet Sample	83
4.3	Microscopic View of Adhesive Cross Section	84
4.4	Descriptive Outline of Adhesive Cross Section	84
5.1	Thermal Gravimetric Analysis of Polyimide Material	85
5.2.a	Specular Reflectance of Fully Coated Sample for 250-2500 nm Wavelength (Perkin-Elmer Lambda-9 Data).	86
5.2.b	Specular Reflectance of Fully Coated Sample for 300-900 nm Wavelength (Perkin-Elmer Lambda-9 Data).	86
5.2.c	Specular Reflectance of Coated Sample	87
5.3	Distribution of Extraterrestrial Solar Radiation	88
5.4	Reflectivity vs. Cone Angle for Coated and Uncoated Samples of Mill Finished Aluminum (at 633 nm)	88
6.1	Schematic Description of Sheet-Forming Apparatus	89
6.2	Relative Difference of Sphere and Parabola	89
7.1	Mold and Air Filtering Equipment	90
7.2	Tooling used for Adhesive Application and Core Transfer	90

7.3	Application of Adhesive to Core	91
7.4	Cross Section of Facet on Mold with Vacuum Bag	91
7.5	Panel Saw Apparatus	92
7.6	Location and Degrees of Freedom of Mounting Hardware	92
8.1	Means of Measuring Contour of 300 mm Facet Samples	93
8.2	Typical Contour Results for a 300 mm Facet Sample	93
8.3	Means of Measuring Contour of Full-Sized Facets	94
8.4	Equipment Used for Some Contour Measurements of Full-Sized Facets	94
8.5	Slope Error (About Y Axis) of Full-Sized Facet	95
8.6	Slope Error (About X Axis) of Full-Sized Facet	95
8.7	Displacement Error of Full-Sized Facet	96
8.8	Surface Analyzer Used to Measure Local Slope Error of Uncoated Facets	96
8.9	Typical Results from Surface Analyzer	97
8.10	Testing of a Full-Size Facet with the Laser Measurement System	97
8.11	Laser Measurement System Description	98
8.12	Repeatability Tests of Laser Measurement for Surface Dimpling	98
9.1	Assembled Facet with all Coatings Mounted in a Display Case	99

Summary

Solar Kinetics, Inc. has developed a design and fabrication technique and demonstrated a honeycomb concentrator facet for space solar dynamic power system concentrators. Solar dynamic power systems require highly reflective and accurate facets in a concentrator to concentrate and focus the solar flux to a receiver. In this effort, the facet is one radial petal of a two-meter diameter parabolic concentrator. It is constructed of adhesively bonded aluminum honeycomb and face sheets with an organic leveling layer coating for improved specular reflectivity.

Fifteen facets were made during this project to develop and refine the fabrication procedure. Each facet was well within one milliradian of a perfect parabola. Optical distortions from honeycomb print-through were successfully addressed by proper matching of the adhesive properties to that of the aluminum face sheets, minimizing adhesive cure shrinkage, and tight control of the quantity and placement of the adhesive during assembly.

A polyimide leveling coating was applied to the bare aluminum face sheet. Aluminum was then deposited on this surface, followed by an aluminum oxide protective film. This provided a specular reflectance of 88%. This is a specular reflectance value through the wavelength ranges of 300-900 nm and 250-2500 nm and is integrated to the solar spectrum. Aluminum was selected for the reflective material rather than silver because of aluminum's resistance to propagation of corrosion.

Analysis of the facets indicate that they will distort only a small amount in the harsh thermal environment of low earth orbit. Initial testing of hardware shows promise for longevity and dimensional stability. Thermal distortion can be minimized by the use of temperature control coatings on the backside of the concentrator.

1.0 Introduction

Solar Dynamic Power Systems are being developed for space electric power production. These systems use solar parabolic concentrators to concentrate and focus solar flux into a receiver where the thermal energy is collected and transferred to a heat engine. The energy conversion efficiency of such systems is dependent on the quality and efficiency of the solar concentrators. High reflectivity and accurate, smooth surface contours allow more solar flux to enter the receiver and increase efficiency. The goal for the concentrator development is to achieve high quality with a low weight durability, and to do so without excessively expensive material or processes.

Solar Kinetics, Inc. (SKI) has developed a design and fabrication technique for an advanced space solar concentrator. The facet is one section of a parabolic dish concentrator. Figure 1.1 shows the basic configuration. The facet is constructed of aluminum honeycomb adhesively bonded to two aluminum face sheets. The front surface is smoothed with an organic leveling coating. An aluminum reflective film is deposited on this surface for high reflectivity, and a thin film of aluminum oxide is used as a protective film. Residual stress is removed by forming the parts prior to assembly. The aluminum sheets are formed into a parabola with a free-form yield process that does not require a rigid tool. The parts are assembled on an accurate mold and then leveled and coated.

This work was performed under direction of NASA Lewis Research Center as Phase II of a Small Business Innovative Research contract. The development resulted from experience gained in the first phase where small-scale uncoated facets were demonstrated.

The objective of this project was to develop a design and fabrication technique and demonstrate an all-metal concentrator facet. The most demanding specification was that of one milliradian (mrad) surface slope accuracy. A high specular reflectance was also required. The facets made during this contract met these objectives. This report documents the work done during this phase, from development of the specifications, to facet assembly and testing.

PRELIMINARY PAGE MARK WITH FILE NO.

2.0 Specifications and Material Selection

The specifications for the facet were established as the first task of this contract. Facet materials were then selected that would best meet these specifications. Setting of the specifications and selection of materials are discussed in this section of the report.

2.1 Specifications (Goals)

The specifications for the facet were developed in conjunction with NASA early in the contract. The specifications were selected as aggressive goals that would provide high concentrator performance. The magnitude of the specifications was based on SKI experience with similar facets and analysis of concentrators with similar configurations.

The specifications that most significantly affect the concentrator performance are those for slope error and specular reflectivity. The following values were selected:

Slope Error	< 1.0 mrad (one sigma)
Specular Reflectance	85-90%

Slope error is defined as the deviation of the surface normal from that of a perfect parabola. Slope error is reported as one standard deviation (one sigma).

2.1.1 Slope Error

One (1.0) mrad was selected as the slope error specification as an aggressive compromise between cost and performance. Total concentrator performance is limited by the fact that the sun is not a point source of light, but rather it is more closely approximated by a disk 9 mrad wide as viewed from near the earth (Ref. 1). The reflected beam is spread due to the width of the sun, even if the concentrator is perfect. Very small concentrator surface imperfections would cause insignificantly small increases in the reflected beam that is already 9 mrad. This relation is shown in the following equation from Jaffe (Ref. 2):

$$\text{beam spread} = [(2 * \text{slope error})^2 + (\text{sun shape})^2]^{0.5}$$

Surface specularity also contributes to solar beam spread, but its contribution has been neglected for clarity. Any solar flux spread (diffuse reflection) due to imperfect specularity would decrease sensitivity to slope error. The factor of two on slope error indicates that error in the surface normal compounds the error of the reflected solar

flux due to the effect occurring on the angle of incidence and angle of reflectance. Figure 2.1 graphically demonstrates this relation. A sun shape of 2.3 mrad (Ref. 2) was used to represent the one standard deviation value of the sun (9 mrad being the full width). The knee in the curve is evident. As is shown, the sensitivity to slope error is small up to approximately one mrad. Beyond that, the beam spread is dominated by slope error.

SKI's experience with other solar concentrators has shown that a goal of one mrad is aggressive, but achievable with the proposed approach. More accurate and costly methods, such as those used for optical mirrors, were not considered.

A similar specification (1.5 mrad) was used by Harris Corp. for the Solar Concentrator Advanced Development (Ref. 3).

2.1.2 Specular Reflectance

Solar energy incident on a concentrator is the sum of the total reflected energy (total or hemispherical reflectance) plus the energy that is absorbed by the concentrator. The total (hemispherical) reflectance is the sum of specular reflectance and diffuse reflectance. Solar radiation usually is described in terms of the solar constant and solar spectral irradiance. The solar constant is the amount of total solar energy received from the sun per unit of time per unit area (normal to the rays of the sun at the mean sun-earth distance) in the absence of the earth's atmosphere. Solar spectral irradiance is the distribution of the solar energy as a function of wavelength (Figure 5.3). Solar reflectance as used herein is defined as the solar weighted value with respect to an air mass of zero.

The specification (goal) for specular reflectance assumed the use of an aluminum reflective film. Aluminum was selected in lieu of silver because of corrosion resistance with the disadvantage of a slightly lower reflectivity. The specification for specular reflectance was based on the theoretical specular reflectance of an aluminum film with a protective film of aluminum oxide (Al_2O_3). High specular reflectance is a prime consideration for a concentrator design. Specular reflectance is reduced by surface asperities (roughness), a very thick and irregular aluminum reflective film and by the protective film. An increase in thickness of the protective film results in a decrease in specular reflectance. Figure 2.2 shows the specular reflectance as a function of the thickness of an aluminum oxide (Al_2O_3) protective film as presented by McClure (Ref. 4). McClure qualifies the exactness of the results because they were based on a "moderately coarse,

piece-wise continuous approximation." In effect, the actual specular reflectance may be higher than that shown. Three other researchers confirm the value for bare aluminum (Ref. 5) (R. Mahoney, 1991, Sandia Laboratories, Albuquerque, NM, Private Communication), (M. Imus, 1991, Optical Coatings Laboratory, Inc., Private Communication), which adds confidence to the values presented. The attainable and experimentally demonstrated specular reflectance with an aluminum oxide protective film is 84.5-88.2%.

The specular portion is of particular importance for solar dynamic power system concentrators. SKI believed and demonstrated that a leveling agent could provide a smooth optical surface to enhance specular reflectance and minimize diffuse reflectance.

2.1.3 Other Specifications (Goals)

Other specifications for the facet are summarized below:

Surface roughness	< 100 Angstroms
Weight	<1.5 kg/m ²
Service life	> 10 years
End of life degradation	< 10%
Space Operating Environment	Low Earth Orbit
Terrestrial Environment	-20 °F to 115 °F
	0 to 100% relative humidity
Structural Loads	Launch and slew

The surface roughness specification is an intermediate specification to specular reflectance and if the reflectance goal is reached, it is of little importance. Weight is an ambitious goal, and is an important consideration for flight systems.

2.2 Material Selection

Five metals were evaluated as candidates for use as the honeycomb and face sheets. They were aluminum, titanium, stainless steel, beryllium, and magnesium. Each was evaluated in terms of dimpling, thermal distortion, mass, and reasonableness of cost.

Table 2.1 provides the significant physical properties of the candidates. The property of importance for dimpling resistance is the tensile modulus, which is a measure of the stiffness of the material. The resistance of the face sheet to dimpling (caused by loads from the adhesive fillet) is proportional to the product of the tensile

modulus and the cube of the material thickness. If the resistance to dimpling is to be kept the same for each material, then the thickness must vary. This relation is shown in the third column from the right. The values in this column represent the face sheet thickness for the specific material ratioed to that of aluminum with equal dimpling resistance. Note that all the candidates except magnesium can have thinner face sheets than aluminum while maintaining the same resistance to dimpling. Although stainless steel can be significantly thinner than aluminum, its density is higher, and the resulting mass is higher also. The relative mass for equal dimpling resistance is shown in the second column from the right. Note that it requires more mass of titanium or stainless steel to resist dimpling than mass of aluminum. Likewise, equivalent dimpling resistance can be achieved with less mass using magnesium and significantly less mass with beryllium.

Each material would have different amounts of distortion caused by temperature gradients through the panel thickness. Such gradients are caused by the portion of absorbed solar radiation on the front surface being transferred to and radiated from the rear surface. High thermal conductivity and heat transfer area will reduce the temperature gradient. A low thermal growth coefficient will reduce the resulting distortion. For samples of equal honeycomb mass, the resulting distortion is approximately proportional to the product of the growth coefficient and density divided by the thermal conductivity. The relative thermal distortion is shown in the far right column in Table 2.1. Note that the distortion of aluminum and magnesium are roughly equal and much lower than that of titanium and stainless steel (300 series stainless). The distortion of beryllium is only 30% of that of aluminum of equal mass. Note that these are approximate values based on honeycomb alone. The effect of the adhesive fillet on the overall thermal conductivity has been neglected. Its influence would reduce the spread of the values but would not change their relative ranking.

From evaluation of these physical properties alone, beryllium is the outstanding candidate. Aluminum and magnesium are of about equal value and are more desirable than titanium or stainless steel.

The cost and availability of the various candidates was reviewed. Beryllium and magnesium sheets are much less common than aluminum; but sheets of the desired thicknesses can be purchased, although their price is prohibitively high. Beryllium sheets are available in 0.020 inch thickness for approximately \$5000 per pound. Beryllium

dust is hazardous to workers' health and shavings are considered toxic waste. This drives up the cost of working with this material. The price of magnesium is reasonable for castings (which are unusable for this application), but unreasonable for sheets. Quotes were received for \$60 per pound for 0.020 inch thick sheets and over \$100,000 per pound for 0.001 inch thickness (needed for the honeycomb core). These prices far outweigh the benefits of reduced weight. Titanium sheets can be purchased for less than \$50 per pound in small quantities. Aluminum and stainless steel sheets can each be purchased for well under \$10 per pound in small quantities.

Based on this review of the materials, aluminum was selected. It provided the best performance of any of the materials that have reasonable prices.

The thickness of the front face sheet was set at 0.012 inch. This thickness was selected as a compromise between dimpling resistance and weight. SKI was conservative in the selection of thickness. It was important to demonstrate high accuracy in this project and reduce the weight in future work. The weight of the final facet was 1.84 kg/m². This includes both face sheets, the core, coatings, and the adhesive. The rear sheet thickness was set at 0.005 inch.

The cell shape of the core was not the typical hexagon of most honeycombs. Rather, the cells were more of a mushroom shape. This allows the core to accept the compound curvature of the facet without significant residual stress. The average cell size for this material was 0.15 inch with a wall thickness of 0.0014 inch.

A polyimide levelling coat was applied over the aluminum face sheet to provide a smooth surface for the reflective mirror. Several options were considered prior to selecting this approach. Diamond turning is one such option. Diamond turning is a machining process that can achieve high surface smoothness. This process has been successfully used for manufacturing mirrors from metal stock for other applications. Typical mirrors are only a few inches in diameter and are over a tenth of an inch thick. The thin, wide material of the facet poses particular problems for our facets. To assess the magnitude of the problem, two face sheet samples were diamond turned. These aluminum samples were 6x6 inches and 0.012 inch thick. The quality of the surface finish was promising, but residual stresses induced by the machining process caused significant sheet warpage (approximately one inch crown). Diamond turning was not

pursued beyond this stage because of the high cost and high risk of development. Risks included the increase in the effect of residual stress as the part size increased. Also, the surface finish quality would decrease as the part size increased. The 36-inch diameter part would exceed the capacity of most diamond turning lathes, and no guarantee of quality could be obtained from the vendors. The cost to investigate this option was driven largely by the cost of a contoured vacuum chuck for holding the part during machining.

Chemically-polished aluminum is a product commonly used for high-efficiency light fixtures, and it has been used for solar concentrators. The performance for commercially available chemically-polished aluminum was not acceptable for our application. The reflectance for a chemically-polished aluminum sheet is shown in Figure 2.3. The reflectance is plotted against the aperture size of the instrument used for the measurement. The low reflectance at small apertures compared to that of large apertures indicates that the reflected beam has considerable spread due to the surface roughness. The wavelength of the light used for these measurements is 633 nm. A curve showing reflectance of the selected coating is shown for comparison.

Epoxy-type levelling layers have been successfully demonstrated for space solar dynamic mirrors. Although some have excellent levelling characteristics, they were not pursued in this work because of their high rate of vacuum outgassing. Polyimides were used instead. A complete description of this coating is provided in Section 5.

The quality of the substrate influences the quality of the leveled surface. Chemically-polished aluminum and mill-finished aluminum were investigated as candidates. The mill-finished aluminum gave the best results. The reflectance of coated samples is shown in Figure 2.4. Each sample was yielded to a spherical shape, coated with the polyimide, coated with a reflective aluminum layer, and then coated with a protective aluminum oxide layer. The wavelength of the light was 633 nm. Although the chemically-polished material initially has a smoother surface, yielding exposes the grain boundaries. This effect appears to be more pronounced with the chemically-polished samples, which makes it a less desirable substrate for our application.

The face sheets were adhesively bonded to the honeycomb core. Soldering and brazing were investigated as alternatives. The most significant advantage of such a

bond would be the dimensional stability provided by the removal of all organics from the structural parts of the facet. Soldering and brazing were tested on small-scale samples. They were never intended to be used on the full-size facet in this contract because of the large development effort that would be required to scale it up to full size.

Titanium honeycomb and face sheets were supplied to NASA Lewis for brazing experiments. These samples were brazed in a vacuum furnace. The brazing material had poor distribution on the titanium and gave inconsistent results. Further improvements to the method were not attempted.

Stainless steel honeycomb and face sheets were soldered at SKI. Solder is similar to brazing except that it is done at lower temperatures. Stainless steel was selected for this demonstration because adhesiveless cores were readily available, and soldering techniques for stainless steel are documented in the literature. Figure 2.5 shows the soldered sample. The solder wicked to the fillet area and provided a bond that appeared to be continuous. Dimpling of the 0.005-inch thick face sheet was difficult to see with the naked eye. These samples were prepared on a hot plate at 500 °F. They successfully demonstrate the potential of mirror structures having no organic materials. Advantages include: lower differential temperature between the front and back face sheets, increased thermal conductivity, less complexity in fabrication and no decrease in optical quality due to age hardening of organic adhesives.

3.0 Thermal and Distortion Analysis

The facet in this development is designed to operate and maintain its accuracy in the low earth orbit (LEO) environment. Transition from sun to shade and shade to sun imposes a transient temperature environment on the concentrator with associated thermal loads. The facet must have the front surface pointed directly at the sun while the back side views earth and deep space. It must also pass in and out of the earth's shadow with a minimum of distortion. The facet is designed for a predicted operational temperature map.

The purpose of this analysis was to predict temperature gradients, bulk temperature swings, and resulting distortion of the facet. The results were also to be used as aids in the development of thermal test limits and in the selection of material manufacturing processes.

During orbit, the front and the back surfaces of the facet see different and varying incident fluxes as it travels in the lower earth orbit. The sources of thermal flux include direct solar, earth thermal, and earth albedo as shown in Figure 3.1. This data is presented as a function of time during the orbit. The orbit geometry is shown in Figure 3.2. The time required for one revolution around the earth is 95 minutes.

The various thermal properties used for the aluminum top skin, bottom skin, and honeycomb core are presented in Table 3.1. This table also presents the thermal properties of the adhesive and the absorptivity and emissivity of the front and back skins.

The emissivity of the rear surface was set at 0.12 because this value produces the lowest temperature gradient between the front and rear sheets, and correspondingly, the lowest distortion. A thermal control coating of aluminum oxide could provide this.

A finite element method was used for the analysis. Half the facet was modelled because it is geometrically and thermally symmetric about the radial centerline. COSMOS/M finite element package was used (Ref. 6).

A detailed finite element model was made of a symmetric portion of a single honeycomb cell with front and back face sheets and an adhesive fillet, as shown in Figure 3.3. The effective heat transfer coefficient and thermal capacitance of the sandwich was then found from this model. These values were used to make a large model of half of the facet called the continuum model. This simplification was done to minimize the size, complexity, and run time of the model.

The model includes the effects of radiation of the outer surfaces of the facet, but neglects radiation within the sandwich. The temperature difference within the sandwich is small (less than 0.5 °C), and internal radiative heat transfer is small relative to conduction.

Steady-state calculations were performed to validate the accuracy of the finite element model of the cell. Absolute temperatures of the face sheets predicted by the two methods were within a few degrees. Temperature drop through the facet was within 30% for the two methods. The finite element model predicted a higher temperature difference. This could be due to simplifications made for purpose of hand calculations.

The effective properties of the sandwich were used in a continuum model. The resulting facet temperature during the orbit is plotted in Figure 3.4. Time zero is defined as the time when the facet enters the shadow of the earth. Front and rear skin temperatures appear as one line because of the relative small difference. The difference is only 0.12 °C at 36 minutes, 0.10 °C at 72 minutes and never exceeds 0.50 °C.

The slope error induced in the facet was calculated at two positions in the orbit approximately corresponding to the minimum and maximum temperatures (time of 36 minutes and 72 minutes). Slope error was calculated graphically from the contour plots of displacement, as shown in Figure 3.5 and 3.6. The X and Y components of the slope error were calculated separately. The contour plot was divided into approximately 30 sections. The slope error for each section was calculated and given a significance proportional to the area of the section. The area weighted error terms for each section were root mean squared for each directional component. The X and Y components were then combined in a root sum squared fashion to obtain one value representative of the slope error of the facet. That value is 1.04 mrad at 36 minutes and 0.49 mrad at 72 minutes. The peak deflection at 36 minutes is -0.015 inch and at 72 minutes is 0.006 inch.

Since the facet bows down at the beginning of the sun phase and up at the end, it passes through zero at some point in between. The slope error likely follows the displacement and decreases from 1.04 mrad prior to increasing to 0.49 mrad. The temperature induced slope error was not analyzed at intermediate times so no mean or effective error can be calculated, although it is likely to be less than one mrad. Note that this error is due solely to temperature changes and must be combined with manufacturing

errors to obtain a measure of on-orbit performance. Arithmetically summing, the temperature induced error and the manufacturing errors would provide a very conservative value, the actual value would be less depending on the nature of the distortions.

4.0 Adhesive Selection and Testing

The adhesive used to bond the honeycomb core to the face sheets is an important element of the facet. Dimpling of the face sheets is dependent on the dimensional stability of the adhesive, and thermal distortion of the panel is dependent on the adhesive's thermal conductivity. The adhesive industry was surveyed to find viable adhesives. A select group of adhesives were tested for dimensional stability. From this group, two of the best adhesives were evaluated further. One of these was then modified, tested, and then accepted for use on the facet.

4.1 Initial Market Survey

The adhesive properties of importance were identified prior to reviewing the data on available adhesives. Minimal shrinkage of the adhesive during cure was weighed as an important property. Such shrinkage would pull the face sheet into each honeycomb cell and cause optical distortions that we call dimpling. Dimpling could also be caused by different amounts of expansion from changes in temperature. An adhesive with a coefficient of thermal expansion close to that of aluminum was required. Typical values are much higher. Most adhesives adsorb and expel moisture depending on the relative humidity of the surrounding air. The resulting swelling and shrinking would also cause dimpling. This is not an issue for operation in a vacuum, but is an issue for terrestrial confirmation. An adhesive that was resistant to moisture was required.

The desired operating temperature range was selected as -67 to 250 °F based on anticipated operational ranges at that time. A high thermal conductivity of the adhesive was desired to limit the temperature difference between the front and rear surfaces. A minimum vacuum induced outgassing was required to provide high dimensional stability and reduce the amount of contaminants that could condense on the concentrator surface or otherwise contaminate space-borne experiments. An adhesive that cured at room temperature was required for two reasons. First, it would avoid the cost and complexity of heated assembly chambers. Secondly, we wanted to cure the adhesive at a temperature in the middle of the operating range so that thermal distortions are not biased in one direction. Room temperature approximated this average. The viscosity of the adhesive needed to be high enough so a significant fillet could be formed, but not so high that a small, well-controlled fillet was impossible. Finally,

the adhesive must have adequate adhesive and cohesive properties. The facets are not highly stressed, so adhesion and cohesion were not the most important properties.

The investigation was limited to two-part epoxy systems. These adhesives are hard when they cure. This is important in order to avoid stress relaxation and distortion of the overall facet.

Manufacturers of adhesives were canvassed to find viable adhesive candidates. Over 65 adhesives from 7 manufacturers were considered based on published data on adhesive properties. Manufacturers' data were typically incomplete and made selection difficult. Manufacturers seldom had information on cure shrinkage and often lacked data on outgassing and moisture adsorption.

4.2 Initial Evaluation

Four of the most promising adhesive candidates were selected for evaluation. Cure shrinkage and humidity expansion were evaluated for each. A thin layer of adhesive was coated on one side of a strip of aluminum. The strip was then hung vertically while the adhesive cured. Shrinkage of the adhesive during cure would cause the strip to deflect with the adhesive on the concave side. The magnitude of the deflection was used as an indicator of the relative cure shrinkage of the adhesives. The strips with the cured adhesive were then placed in a high humidity environment. The resulting change indicated the relative response to moisture.

4.3 Extended Adhesive Evaluations

From the results of the initial evaluation, two specific adhesives were chosen for extensive testing. These adhesives will be referred to as adhesive A and B.

Small flat facet samples were made using each of the two adhesives. Adhesive A had the smallest cure shrinkage and smallest response to moisture adsorption. However, the bond strength decreased substantially after a few weeks, and the facets could not withstand moderately rough handling. Manufacturer suggested modifications did not improve the adhesion, so adhesive A was eliminated from consideration.

The facets with adhesive B also failed, but the failure was in the adhesive itself rather than the interface between the adhesive and aluminum. Adhesive B was an epoxy resin with an aluminum filler. We decided to eliminate the

aluminum filler and start with the base resin. This adhesive resin was modified to improve those properties that affect surface accuracy without forfeiting much strength. SKI wanted to reduce cure shrinkage, reduce the coefficient of thermal expansion, and increase the thermal conductivity.

Evaluation of different modifications was done by using the adhesives to assemble 150 mm (6 inch) square facets. These facets were used for ultrasonic tests of bond continuity, humidity and temperature cycling, and dimpling evaluation. Fabrication of these samples was quick, simple, and proved to be an accurate means of evaluation.

By adding mineral fillers, mechanical properties can be enhanced while properties such as thermal expansion can be controlled. With this in mind, a high-purity alumina powder was added to the adhesive. Specifically, a 20% (by volume) 0.05 micron powder was used as the filler. A notable decrease in cure shrinkage could be seen in the form of dimpling in 150 mm square facets. The addition of this filler would also increase the thermal conductivity, while reducing cure shrinkage.

At this point, a concern for the bond at the filler/matrix interface was addressed. A poor interface would be a means for microscopic crack initiation and propagation that could result in adhesive failure.

In order to alleviate the filler/matrix interface problems, an organofunctional silane was added. The intention was to chemically bond the epoxy to the alumina filler, thereby increasing bond strength and reducing the tendency for crack initiation at the filler/matrix interface.

Organofunctional silanes are chemically structured to couple inorganic fillers to organic polymers. Several types of silanes were available, and one was specifically selected for the materials to be coupled.

Mixing of the catalyst, resin, filler, and organofunctional silane was done in the following sequence: the silane (approximately 0.75% of total mixture weight) was mixed thoroughly into the resin, filler was then stirred in, and followed by the catalyst. Total elapsed time for this process was typically 30 minutes. However, for process times much over an hour, it was recommended that the silane be added to the filler or catalyst first, in order to increase the pot-life of the components prior to mixing. Since process times at SKI never exceeded 45 minutes, this was not a concern.

Results of all tests of the modified adhesive B were deemed acceptable. No noticeable decrease in bond integrity occurred for the duration of the tests. This was based on qualitative examination of facets under large bending loads. Failure always occurred in buckling or yielding of the facet sheets, rather than bond failure. Although dimpling was evident prior to and during the tests, no anomalous changes were noted through any of the humidity or temperature cycling.

The rate of vacuum outgassing for the final formulation was calculated based on manufacturer's data for the same resin with almost equal amount of aluminum (rather than alumina) filler. The expected outgassing rate is based on a total weight loss of 1.3% at 260 °F and 10^{-5} torr for 24 hours. This is higher than desired. Typical goals for flight components are less than 1% total weight loss.

4.3.1 Humidity Cycling

The purpose of humidity cycling was to demonstrate the resistance of the facet to degradation in adverse environmental conditions during facet storage. For this testing, several 12 mm x 100 mm facet strips were subjected to humidity cycling.

A cycle was defined as approximately 8 hours at a relative humidity of 100%, and from 16 to 48 hours at ambient humidity of the laboratory. Temperature was relatively constant at 75 °F. Relative humidity of 100% was maintained by means of a water vapor humidifier ducted into a small test chamber. The saturation point was continuously exceeded and resulted in heavy condensation in and on the facet. Ambient humidity varied from 10% to 80% throughout the testing. A sample was removed from testing every eight cycles for destructive testing to determine if and when a failure would occur.

No significant decrease in bond strength was noted for any sample experiencing 25 cycles or less. Humidity cycling was discontinued at this point.

4.3.2 Temperature Cycling

A 100 mm square, flat facet was used for the temperature cycles. The cycles were defined as approximately 6 minutes at temperatures over 90 °C but not exceeding 105 °C, and the remainder of the time cycling between 37 °C and the upper temperature limit. Total elapsed time for one cycle was typically 40 minutes.

Since the facet would be expected to complete tens of thousands of temperature cycles during its active lifetime of several years, an accelerated aging test was difficult to accomplish. However, over 4000 cycles were completed prior to the end of the contract with no notable decrease in mechanical properties of the adhesive. A slight discoloration of the adhesive became apparent after a few hundred temperature cycles. This was expected since benzene-type rings in a chemical structure will cause discoloration after high temperature exposure.

4.3.3 Ultrasonic Test Results

The ultrasonic tests were done by immersion of a 150 mm square facet in a water bath. The ultrasonic probe and receiver were placed on either side of the facet, and ultrasonic waves were reflected or transmitted through the facet. Ultrasonic results of an early sample (150 mm square) are shown in Figure 4.1. Dark areas indicate poor transmission through the part, which would indicate incomplete bonding. Since the ultrasonic tester could not resolve bond discontinuity much less than the cell size, a combination of cell openings and continuous bonds along the wall resulted in a gray area. The white area at the bottom of the facet was caused by water leaking into the core. The edges were sealed for these tests with tape, and initial samples had significant leaks.

Figure 4.2 shows the results of a later sample. The light and dark gray areas almost cover the part. Local dark areas near the right-hand edge were of unknown origin. The face sheets were peeled from this facet so these bonds could be visually inspected. No anomalies were evident with the naked eye. It is suspected that the dark region is caused by slight variations in the thickness of the core (note that the dark region follows the direction of the core ribbon) that would alter the local distance between the heating metal parts.

4.3.4 Microscopic Inspection

Several facet cross sections were prepared metallographically and examined with a scanning electron microscope. Figure 4.3 shows a typical section of the bond area. Note the gap between the core wall (vertical) and the inner surface of the face sheet (horizontal lower part of photo). Of the twelve samples measured, this gap ranged from 0 to 0.0026 inch, with an average of 0.0008 inch.

The examination also provided detailed measurements of the fillet size and shape. The outline has been traced and

presented in Figure 4.4 for better clarity. The average height of the fillet on the cell wall was 0.039 inch (0.020 inch minimum and 0.075 inch maximum). The width of the wetted surface on the face sheet averaged 0.038 inch (0.025 inch minimum and 0.063 inch maximum).

5.0 Coatings

The surface roughness of the metal face sheet, as it arrives from the mill, is several orders of magnitude higher than is tolerable for concentrator surfaces. Chemically-polished aluminum is much smoother, but not acceptable for these applications. Chemically-polished aluminum, front skin, when subjected to a forming operation, will expose the grain boundaries. This was confirmed by placing some samples under such conditions. The grain boundaries were exaggerated under the forming stress. This, in turn, led to the increase in surface roughness of the front face skin. SKI chose to apply a polyimide leveling agent to the surface of aluminum sheet. This layer provides the smooth surface for deposition of an aluminum reflective coat and an aluminum oxide protective coat.

Polyimides possess a highly aromatic ring structure and as such have exceptional thermal stability even at temperatures of 500 to 600 °C for short periods of time. They belong to a new group of plastics with the highest thermal stability developed to date.

The polyimide used is from a family of liquid organic polyimide coatings used in the semiconductor industry for wafers, chips, or other substrate applications. These coatings offer many performance and processing advantages and improve long-term reliability for IC devices. This organic leveling agent outperforms inorganics such as oxides in planarization, coating ease and versatility, and mechanical, thermal, and environmental protection. And because it provides a smooth, virtually pinhole-free surface over topography, it does improve the surface smoothness before the mirrorizing of the surface. This leveling coat is spin-coated and cured at a low temperature (210 °F). Also, it can be easily etched and stripped and requires few processing steps. The coating could also be applied by spraying or roller coating depending on size and the surface to be coated.

The technique used for this application is proprietary, but is similar to standard photo resist spin coating techniques. This process is adapted to coat large surfaces. It provides uniform, pinhole-free coatings and can be controlled in thickness between 5,000 and 35,000 Angstroms. Most development work done, to date, in semiconductor applications has used 3 and 4 inch wafers. In the development effort undertaken within this contract, uniform leveling coating has been achieved on substantially larger surface areas.

Spin coating is a standard process for applying reproducible, uniformly thin (micron) coatings to substrates. The two main current applications for spin-on coatings are photoresists used in the processing of integrated circuits and inter-layer dielectric polymers such as polyimides used in the fabrication of multilayer thin-film circuits. In semiconductor device manufacturing facilities, spin coating is part of the automated in-line production process.

The first step in spin coating consists of placing the substrates on a motor-driven rotary vacuum chuck mounted in a bowl. The coating is then dispensed onto the center of the substrate, and the spinner turned on, causing the coating to be evenly distributed by centrifugal force. In general, excess solution is used to assure good substrate coverage. The resulting coating thickness is a function of the solution viscosity and the spinner speed. A thicker coating can be obtained by increasing the viscosity of the solution or reducing the spin speed or both. Typically, thickness is a hyperbolic function of the spin speed; thinner coatings are obtained at higher speeds. Regulation of these parameters allow control of coating thickness.

Typically, substrates most often used for spun-on coatings are circular silicon wafer, although square or rectangular substrates can also be used. In the latter cases, coatings are thicker at the edges and corners, and the uniformity is harder to obtain.

Each one of the following variables affects the uniformity and overall quality of the final film and is controlled to obtain consistent results:

1. Facet surface preparation - cleaning.
2. Adhesion promoter (if required).
3. Dispensing.
4. Spin Speed.
5. Cure.

The outstanding properties of polyimides include the following:

1. High-temperature oxidation stability and low weight loss.
2. Temperature stability from -190 to 300 °C.
3. Flame resistance (since polyimide will not support combustion in air and will ignite only at temperatures above 400 °C).
4. High-wear resistance.
5. High-radiation resistance.
6. High-chemical and solvent resistance.

By far, the most valuable property of the polyimide polymer and the reason they are replacing many other materials is

their high-temperature stability and their retention of physical properties at high temperatures. Practical continuous service temperatures range from 150 to 300 °C, with stability up to 600 °C for short periods of time.

The thermal stability of polyimides has also been demonstrated by the use of thermal gravimetric analysis (TGA). Figure 5.1 shows the weight loss of a sample as a function of temperature. The heating rate was 20 °C per minute. The solid line represents weight percent of the sample. The dashed line represents the rate of weight loss. The near zero rate of weight loss up to a temperature above 300 °C shows the stability in the anticipated operating range (less than 100 °C).

The resistance of polyimide coatings to organic solvents, moisture, and synthetic lubricants and greases is very high. Only slight deterioration occurs when polyimides are immersed up to 4 weeks in organic solvents including ketones, alcohols, aldehydes, chlorinated solvents, benzene, and haphtha. The resistance of polyimides to strong acids and bases is, however, not as good as its resistance to organic solvents.

Aluminum was selected as the reflective material in the proposal phase of this work because of its resistance to corrosion in an atomic oxygen atmosphere. Silver corrodes rapidly when exposed, although it has better initial reflectivity.

Aluminum oxide was selected as a protective coat for the aluminum based on its good compatibility with aluminum and its superior scratch resistance as compared with magnesium fluoride. The aluminum and aluminum oxide coatings were both deposited by vacuum vapor deposition. The thickness of the aluminum oxide was 1000 Angstroms.

Table 5.1 summarizes the properties of the coatings.

The issue of importance for a solar concentrator is a high specular reflectance and low diffuse reflectance. A number of reflectance measurements were made of developed experimental test samples which would duplicate the final product, both in materials and fabrication technique.

Hemispherical, specular and diffuse reflectance were obtained using a Perkin-Elmer Lambda-9 UV/VIS/NIR spectrophotometer operated with a 60 mm barium sulfate coated integrating sphere. Integrated solar reflectance was obtained by measuring the spectral reflectance over the wavelength range of 250-2500 nm, and convoluting the

spectrum into the air mass zero solar spectrum over the same range. This spectrophotometer has a 230 x 320 mrad specular reflectance aperture (approximately 0.9 steradian). The spectral reflectance uncertainty is $\pm 2\%$. Three different areas were scanned on each sample.

The hemispherical (total) and diffuse spectra were measured through a wavelength range of 250-2500 nm and 300-900 nm. Specular reflectance was determined from these measurements. Solar integrated values for each scanned region were determined. The integrated solar specular reflectance was determined to be $88.3 \pm 0.1\%$, and the integrated solar diffuse reflectance was $1.1 \pm 0.2\%$. Measurements were made with two (2) separate Perkin-Elmer Lambda-9 units and were in agreement for both units.

Specular reflectance at a wavelength of 660 nm was also obtained using a "Devices and Services" 15R portable specular reflectometer operated with a 25 mrad specular receiver aperture. Five reflectance readings were obtained. The specular reflectance at 660 nm of Sample X-1 was determined to be $87.4 \pm 0.1\%$ using this technique. This value is slightly lower than the integrated solar specular value obtained on the Perkin-Elmer Lambda-9 units since the receiving aperture on the Portable Specular Reflectometer is much smaller than on the Perkin-Elmer Lambda-9 unit. The accuracy of the portable unit is lower than Perkin-Elmer Lambda-9 unit. The results of the measurements are shown in Figures 5.2.a and 5.2.b.

Measurements were also made using a modified Varian CARY 17D spectrophotometer. The instrument is typically used for measuring transmissivity of samples. Three reflective samples of the same material were mounted in the instrument such that the incident beam was reflected from each into a detector. The intensity was recorded as the wavelength of the incident light was varied over the solar spectrum. The specular reflectance was measured by reflecting a laser beam off a specimen through a small aperture into a detector. The aperture was sized to accept only the reflected energy that spread less than 2 mrad from the beam center (4 mrad of full cone). These measurements were made at a wavelength of 633 nm. All the values recorded from the measurements using the large aperture were adjusted based on the relative difference of the specular and diffuse values at 633 nm. This gives the specular (4 mrad) reflectance as a function of wavelength as shown in Figure 5.2.c. Reflectance values from this unit appear to be consistently lower than the reflectance measurement values obtained from the Perkin-Elmer Lambda-9 units and the Devices and Services 15R portable specular reflectometer. The difference is likely

due to the much smaller aperture (4 mrad vs. over 230 mrad), but may be attributed to the accuracy or sensitivity of the unit.

Figure 5.3 shows the distribution of solar radiation as a function of wavelength. The solar intensity is much higher in the wavelength range from 400 to 700 nm than at other wavelengths. Accordingly, the reflectance in this region is more important. To determine the solar reflectance, the curve in Figure 5.3 is integrated and multiplied by the specular reflectance values from Figure 5.2.a. This yields a single value that represents the solar weighted reflectance of the sample. For the sample measured, the solar weighted reflectance within a 4 mrad full cone angle was 85.8%.

The reflectance was also measured as a function of the cone angle for coated and uncoated samples. These results are shown in Figure 5.4. The wavelength for these measurements was 633 nm. This visually demonstrates that an improved surface is achieved with the polyimide leveling coating.

A full set of reflectance measurements was not performed on each facet because the spectrophotometer is limited to small sample sizes. The specular (4 mrad) reflectivity at 633 nm was measured on each facet. This value was compared to the same measurement on the sample characterized previously in Figure 5.2.c. That value was 84.7%. If the specular reflectance of the facet at 633 nm exceeded 84.7%, then it was assumed that the solar weighted reflectance exceeded that of the previous sample (85.8%). The data shown in Figure 2.3, 2.4, 5.2.c, and 5.4 were obtained with the Varian Cary 17D spectrophotometer and laser/small aperture unit. The reflectance (633 nm with 4 mrad full cone angle) of the five coated facets were 86.5, 86.1, 85.9, 84.0, and 84.2%. Two facets had values less than the sample, but not more than a percent less. The 85.8% reflectance of the sample exceeded the goal of 85%, but only by a small margin. These differences fall within the likely uncertainty of the measurements. The conclusion from this work is that samples and facets have been made that meet the reflectance goal, and some facets had reflectances very close to, if not exceeding, the goal.

Contamination of the leveling coat by particles of dust is quite apparent after the reflective coating is applied. Sharp local distortions in the reflected image are easy to find. The first facets had substantial number of such particles. The cleanliness of the coating operation was improved, and the number of contaminants dropped. The final facets averaged one to two visible particles per facet.

These imperfections have negligible impact on performance because of their size and can be further reduced with upgrades in the facilities.

The coating of one facet was destroyed while the facet edges were being trimmed. The adhesion between the reflective aluminum coat and the polyimide on that facet was poor. This allowed the aluminum and aluminum oxide layers to peel away from the facet at a few locations. No similar experience occurred with the other facets. This indicates that the repeatability of the coating process needs improvement.

The imperfect leveling coat on some of the initial facets was removed and new leveling coats applied. The coating was removed chemically and some etching of the face sheet occurred. This increased the surface roughness of the face sheet and apparently decreased the effectiveness of the polyimide leveling coat. Facets that were stripped and recoated had specular reflectance values well below that of the initial coating due to resultant surface roughness. The significance of this issue is believed to be small since it is peculiar to prototype development. Increasing the thickness of the leveling coat may eliminate the surface roughness.

6.0 Sheet Forming

Forming of the front and back face sheets, prior to facet assembly, was introduced early in the contract as a means of reducing residual stresses in the facet. The residual stresses were detrimental in that the facet would have a tendency to creep towards the face sheet's original, unstressed shape.

Forming was done by clamping the edge of a sheet with two circular flanges and applying uniform pressure to its surface. This is illustrated in Figure 6.1. Sheets were laid on the bottom half of the flange, the upper half was lowered, and equally spaced bolts were placed circumferentially and tightened to clamp the sheet. A pressure port in the bottom half was used to pressurize the plenum erected between the sheet and flange.

Control of the magnitude of forming was initially done by monitoring the displacement of the face sheet center. However, actual contour measurements were determined to be a more effective and accurate way of controlling the shape. Several variables such as creep during forming, material defects, and sheet thickness tolerances resulted in slight contour variations for sheets that had similar center displacements. A four-point contour gauge measured the surface contour of the membrane at intermediate stages during forming. Forming was stopped when the desired contour was reached.

Sheets for the 300 mm sample facets were formed on flanges with an inside diameter of 460 mm, and sheets for the full-size facets were formed on 920 mm diameter flanges.

Typical forming pressures on either flange were 9 - 13 psi for .305 mm sheets and 1.5 - 2.5 psi for .127 mm sheets. Contour measurements for both sheets were taken at a reduced pressure of one psi.

An outline of the part was drawn on the sheet to be formed. The face sheet was drawn approximately 20 mm oversize. The back sheet was drawn approximately 10 mm oversize. After forming, the front and back sheets were removed from the flange and trimmed by handheld sheet-metal shears.

The sheets would need to be formed to a parabola to remove all of the residual stress. The shape achieved with the technique described here is a close approximation to a parabola, but it is actually better defined by a sphere. The difference causes the sheets to have an imperfect fit when rested on the parabolic mold. The vacuum pressure used during assembly draws the sheet to the mold. The

residual stress created by this process is believed to be small. Analytical data indicates that a sheet could be formed to a spherical contour that would be within 10 milliradians (rms) of the ideal parabolic contour. This demonstrates how close the two shapes are. Figure 6.2 illustrates the results of a two-dimensional analysis of a parabolic versus spherical profile. The data is the difference in slope as a function of radial position for a spherical surface as compared to a parabolic surface. It is assumed that the displacement at the end points of both the sphere and parabola are coincident.

Aluminum sheets formed on the 450 mm diameter flanges did not have a continuous spherical curvature. Boundary restraint at the clamping zones resulted in bending stresses and variations in circumferential tensions. Formed sheets had circumferential displacement errors of approximately 1.3 mm when laid on a spherical mold of 2150 mm radius. However, these errors were considered representative of errors that would be seen when laying full-size spherically contoured sheets on the parabolic mold. Typically, sheets formed on the 450 mm diameter ring have spherical curvature within 120 mm from the center of the ring and flatter zones outside this region. The actual shape of the formed sheet, therefore, resembles a bell shape rather than a true hemisphere.

A similar effect was seen with the larger sheets. The deviations from true spherical contour were even advantageous when attempting to simulate a parabolic shape. The slope errors illustrated in Figure 6.2 could be reduced near the outer boundary of the parabola by this effect. Therefore, the flatter zones could be utilized where needed and avoided where greater slope was required.

7.0 Facet Fabrication

Assembly of the facets required many specialized steps: each one carefully controlled. The facet sheets were first formed to shape using a free-form yield process. They were then chemically cleaned for adhesion and assembled on an accurate contoured mold. The assembled facet was then coated with the leveling agent, reflective film, and protective film. The final steps in the process were trimming of the facet to size and attaching mounting hardware. This section of the report discusses these steps in detail. Because of the importance of surface preparations, it is discussed independently as the first subsection.

7.1 Preparation of Surfaces for Facet Fabrication

It is important to carefully clean and thoroughly prepare the surfaces of aluminum front and back sheets. Thus, before the lay-up of the front, the adhesive screen printed honeycomb core and the back sheet are all prepared.

The front and back face sheets are thoroughly cleaned in a 1,1,1-Trichloroethane vapor degreaser. As these materials are of mill quality and finish, they have non-uniform oxide buildup and processing lubricants and soil. Vapor degreasing is a physical method of removing solvent soluble oils and soils from the nonporous surface of aluminum.

By bringing the face sheet at room temperature into contact with hot solvent vapor, the vapor condenses to a liquid on its surface. Sufficient liquid solvent is formed to carry the soluble and insoluble soils away as the solvent drains by gravity.

The solvent vapor degreaser is a tank with a heat source to boil the solvent and a cool surface to condense the vapor in the upper section. The face sheets are suspended in this air-free zone of solvent vapor. The hot vapor condenses onto the cool part dissolving oils and greases providing continuous rinse in clean solvent.

As the condensed solvent drains from the part, it carries off the soils and returns to the boiling liquid reservoir. This vapor treatment is often augmented by mechanical action of spraying the sheets with the hot solvent, with liquid solvent beneath the vapor level. The sheet is held in the vapor zone for final rinsing until the parts reach vapor temperature, at which time the condensation stops. The sheets dry immediately within the machine as they are withdrawn from the vapor. The process is a safe, rapid, economical procedure for preparing the face sheets. This process does not produce a surface that will pass the

"water-break" test. Thus, for our cleaning requirements that necessitate essentially complete freedom from water-soluble, solvent-soluble, and chemically combined contaminants, vapor degreasing is followed by water rinsing to remove traces of water-soluble soils and chemical etching (oxidation and reduction steps) to remove oxides from the surface.

The "water-break" test is used to detect the presence of organic contaminants on the metal surface. This test indicates a hydrophilic surface rather than cleanliness. The surface is immersed in a tank of deionized water (or tap water free of contaminants), removed vertically, and the draining water film observed. Uniform and continuous wetting indicates absence of organic material on the surface.

On a surface with organic (hydrophobic) matter, the water film will tend to break up and withdraw into wetted areas and expose areas not wetted.

If the surface is free of hydrophobic materials, the water film drains as a thin, uniform layer. The presence of wetting agents in the water or on the surface will give erroneous results.

Thus, chemical etching is a suggested surface preparation prior to adhesive bonding. Various acid etching processes for removal of oxide coatings and mill finishes have been used in the aluminum industry. The method used by SKI is the sodium dichromate-sulfuric acid etch, and it has proved to be an effective surface preparation method.

The sulfuric acid, sodium dichromate etch is done in specially fabricated high-density polypropylene (HDPE) tanks that can accommodate a full-size facet sheet and honeycomb core in vertical hanging position. HDPE was chosen because its neutrality and stability to acids. The etching solution consists of 22 percent by weight of concentrated sulfuric acid, 4.4 percent by weight of chromic acid salt, and the balance is deionized water. Ten grams of 2024-T3 aluminum was added as seeding material due to presence of copper in the alloy. To keep the level of etching to the minimum and avoid pitting, this solution was used at room temperature (77 °F).

Compressed air is bubbled through this solution to help with the etching by agitating the solution. During transfer of the components from the etch tank to rinse tank, the part is continuously sprayed to keep the part wet. It is important to keep the part wet or else the acidic salts will cause localized pitting on the surface. The part is immersed in the rinse tank for 30 minutes. The

pH of this tank is maintained above 3.0 to avoid potential poor adhesion if highly acidic water dries on the part.

The rinse tank is of the same high-density polypropylene construction as the etch tank. The tank is large enough to accept the largest part to be rinsed. The rinse water is changed frequently to remove the contaminants and acidic salts coming from the surface of the facet face sheets.

Rinses were thorough to minimize the contamination and eventual pitting (corrosion) of the face-skin surfaces.

7.2 Facet Fabrication Procedures

Fabrication of 150 mm square, 300 mm square contoured, and full-size facets is done by virtually the same procedure. Therefore, procedures for all facets will be discussed in the following section as one unique procedure.

Sheet forming for 300 mm and full-size facets was done prior to any cleaning or fabrication procedures. Sheet forming for 300 mm and full-size facets was discussed in the previous sections and will not be included here.

7.2.1 The Panel Fabrication Work Area

All panel fabrication processes were done within the confines of a room that was maintained with a cleaner environment than the surrounding office and machine shop work areas. Suspended ceiling tiles were modified to have an aluminum surface for eliminating dust from the ceiling. The supply air duct was filtered and the return duct blocked off to create positive pressure within the room. Filters were changed and the room cleaned weekly. Dust-free rubber gloves and lint-free lab coats were worn while working in the room. A separate chamber outside the working room was used as an interlock for preventing dust from entering through doorways.

It was discovered in early fabrication trials that mold contamination by air-borne particles would become an issue. Lint or dust particles approximately 10 microns (0.0004 inch) in size were being trapped between the mold and face sheet. The particles would create "divots," which were typically 10 mm in diameter and 10 microns deep. The localized errors had approximately 2 mrad peak error and were visually distracting. Initially, the areal density of these imperfections was 80 to 120 per square meter. Attempts at reducing the areal density by wiping the mold and face sheets with lint-free cloths immediately prior to laying down the face sheets could not significantly reduce the number of divots.

The next step was applying a tacky pre-mask to the mold and optical side of the face sheet. The face sheet was placed on the mold and both pre-masks were removed simultaneously. This process reduced the area density of the divots to 20 to 40 per square meter, but was extremely cumbersome for the larger facets. Thus, a cleaner work space became a requirement.

To meet this requirement, a low-profile, lightweight, laminar flow unit was used. This unit was equipped with HEPA filters capable of filtering 0.3 micron particles with 99.99% efficiency. The unit was suspended from the ceiling above the mold and operated continuously. See Figure 7.1.

The mold was cleaned thoroughly with lint-free cloths while under the laminar flow unit. Therefore, air-borne particles were not allowed to collect on the surface while the unit was operating. With this process, the size and quantity of the divots were reduced. The area density of the divots was reduced to less than 6 divots per square meter or one to two divots per facet. This represents less than one percent of the area (0.05%) and has no significant impact on optical performance. Further reduction in the number of divots to improve appearance could likely be obtained by enlarging the area around the mold that has filtered air.

7.2.2 Placing the Face Sheet on the Mold

In order to prevent trapping air-borne particles between the face sheet and mold, the face sheet must also be cleaned under the laminar flow unit. First, the face sheet was held upside down and the optical side wiped thoroughly with isopropyl alcohol and lint-free cloths. It was then slid under the laminar flow unit and tilted to allow the air stream to blow particles off and away from the face sheet and mold.

The sheet was then placed on the mold in the proper orientation. Polyethylene tape was used to hold the face sheet down and prevent vacuum leaks. Since the face sheet was cut approximately 20 mm oversize, there was not a problem with overlapping the tape. After all edges were sealed, face sheet vacuum was applied. The vacuum was then increased until all air pockets between the face sheet and mold were evacuated. Typically, this vacuum reading was 150 - 200 mm Hg. The reading was recorded, and the vacuum was increased to approximately 400 mm Hg and later reduced after the rear sheet was in place.

7.2.3 Transferring Adhesive to the Core and Core Transfer to the Mold

To apply the adhesive to the core in the required thickness, the adhesive was first spread on a flat sheet, and the core edge was then dipped into it. Adhesive was poured on two separate glass plates with transparent mylar sheets used as disposable covers. A wire frame was placed on the glass, and a 125 mm wide putty knife was used to spread the adhesive to a thickness that closely approximated the wire diameter (0.46 mm diameter on 38 mm centers). See Figure 7.2. When the wire frame was removed, the adhesive settled and created a thickness of approximately 0.38 mm.

The next process involved setting the flexible core in the adhesive on one of the glass plates. The mating glass plate was then aligned and placed on top of the core to create a sandwich structure (see Figure 7.3).

The glass plates were clamped in this position and rotated for visual inspection. Areas that had poor adhesive transfer or contained contamination were easily inspected in this manner. Then the sandwich was rotated back to its original position, and the clamps and top plate were removed. The laminar flow unit was turned off at this time to prevent handling problems when placing the core.

To transfer the flex-core to the mold, tooling with suspended clips was placed over the core. The clips were then attached to the core at locations near the edge (this step was replaced by handling with tweezers for the 150 mm facet, due to its small size). The core was then lifted from the glass plate and moved to the face sheet on the mold. The core was carefully aligned above the face sheet, lowered, and the clips detached.

7.2.4 Placing the Back Sheet

After the core had been placed on the face sheet, the back sheet and vacuum bag were prepared for placement. If the back sheet had undergone excessive handling, a thorough isopropyl alcohol wipe-down was done followed by a 10 minute blow-dry with a heat gun prior to any facet fabrication procedures. The back sheet was placed on the core followed by the vacuum bag on the back sheet, as shown in Figure 7.4.

Vacuum pressure was increased on the back sheet until uniform contact was made between the back sheet, core, and

face sheet. This level was typically 100 - 125 mm Hg. The level was then increased by 25 mm Hg to account for a margin of error.

At this point, the face sheet vacuum was decreased to approximately 250 - 325 mm Hg. This supplied just enough differential pressure to maintain contact between the mold and the front sheet without forcing the face sheet to follow small irregularities in the mold surface.

All vacuum levels were maintained for the duration of the adhesive cure cycle. This ensured contact at the face sheet/mold interface during adhesive cure and also evacuated outgassed products that were produced during the cure cycle.

7.2.5 Mounting Tooling Alignment

Prior to facet removal from the mold, the facet was marked for mounting tooling attachment and edge trimming.

Water-based ink was used for any marking within the specified part size. Scribing was used as the method of marking the boundaries of the specified part. The permanency of these scribe marks was critical, since duplication of the exact position of the facet on the mold was difficult after facet removal.

Locating the specified part boundaries was done by transferring the part lines on the mold to the back side of the face sheet of the facet. From these scribe lines, a geometric center of the part could be determined.

The mounting tooling locations were determined by overlaying a template on the back side of the facet. The template was referenced to the geometric center and radial centerline of the facet. Mounting points were located on a 25.4 cm (10 inch) radius from the geometric center.

7.2.6 Edge Trimming/Sealing

Upon completion of the coating processes, the facet was prepared for edge trim to specified part size. A heavy-duty parabolic facet was made to support the facet during trimming. This support facet was made from .508 mm (.020 inch) face sheet, .305 mm (.012) back sheet, and pressure-formed rigid honeycomb.

The backing facet was mounted on stacked rotational and translational tables that could be positioned to achieve any desired linear cut within the oversized part. The

oversized facet was then mounted to the backing facet by clamps and low-density polyurethane load distributors. These clamps and load distributors were positioned not to interfere with the desired cut.

The entire positioning and clamping setup was mounted atop the cutting tool section of an engine lathe. The lathe provided a means of controlled feed-rate of the facet under the facet saw. The optimum feed-rate was 80 mm/min. Feed-rates much higher than this resulted in excessive vibration in the facet. Feed-rates much below this resulted in some localized heat buildup at the facet edge.

The facet saw consisted of a 50.8 mm diameter high-speed steel jewelers' slotting saw blade. Thickness and teeth per blade were .406 mm and 190, respectively. The saw blade was used with a 25,000 rpm router that was mounted on a rocker arm. This allowed the panel saw to follow the contour of the facet while maintaining a linear cut. Figure 7.5 shows the panel saw. The router is near the center with the pivot arm attached to the top. The backing facet can be seen on the lower left of the photograph.

The depth of the cut was maintained by a small rubber wheel positioned beside the saw blade. The height of the wheel could be set and locked in any vertical position. Material was removed from the cutting blade by a steady air flow from an air line positioned behind the blade. The air flow also aided in dissipating heat from the blade and facet during cutting.

The facet was then removed from the saw table and prepared for the edge seal. The purpose of this final edge seal was for rebonding any localized edge delamination that could have occurred during edge trimming. For this process, the adhesive was used without the addition of any fillers. Since the unfilled adhesive had lower viscosity, it had the capability of filling small cracks by capillary action.

Compressed gas was used to remove microscopic particles from the edge prior to any adhesive application. The facet edge was then dipped in a measured thickness (0.38 mm) of adhesive. Compressed gas was again used to ensure that no venting slots were clogged. Excess adhesive was wiped from the face and back sheets with isopropyl alcohol, and the adhesive was allowed several days to cure.

7.2.7 Mounting the Support Hardware

Support hardware was attached to the back of the facet in three locations to support the facet for display and measurement. A fastener system that would allow growth by

thermal expansion while restraining the facet in translation was constructed. Small swivel adapters were placed at three specific locations on the facet. These swivel adapters were small spherical bearings that allowed rotational movement only. Mounting locations and axes of movement for each point are shown in Figure 7.6. Each individual swivel adapter is mounted on a stand that restricts movement in certain axes. Point 1 was fixed and did not allow translational movement. Point 2 was a hinge that allowed movement through one axis only. Point 3 was a swivel that allowed 360° of translational movement.

The facet is coated with the leveling layers and the reflective and protective films prior to being trimmed. The coating technique leaves excessive polyimide at the edge of the front sheet. This area is completely removed by trimming.

8.0 Measurement of Facet Slope Error

Facet slope error measurement methods were separated into two discrete systems. Slope errors that had periods of greater than 19 mm were measured by a coordinate measuring machine (CMM). A cursory measurement of all facets was done by a SKI-manufactured CMM that acquired data on a 38 mm grid. This measurement system was not intended for use as a final acceptance process, but rather a method of screening facets for fabrication errors, or errors occurring prior to and after environmental testing.

Slope errors that had periods less than 19 mm were measured by (1) a mechanical contact surface analyzer prior to coatings and (2) a laser measurement system after the coating and films were applied. Surface roughness with small periods (approximately 1.8 mm) was characterized as specular errors and could be measured with a specular reflectometer.

Data acquisition and reduction methods for the CMM of the 300 mm and full-size facets were defined separately. Therefore, 300 mm and full-size facet slope error measurements will be discussed separately. Surface analysis and reflectivity measurement techniques were alike for all facets and will be discussed as one topic that encompasses all facets.

8.1 Measurement of 300 mm Spherical Facet Slope Error

Measurement of slope error in the 300 mm facets was done in a polar coordinate system. The measurement system consisted of a rotating table mounted atop a linear slide. The rotation table and linear slide provided the radial and circumferential independent variables; respectively, while deflection in the vertical axis was considered the dependent variable. Deflection in the vertical axis was measured by a dial indicator suspended above the facet. This system was designed to provide information on the effect of intrinsic stresses on slope error as well as information on process variables associated with facet contour. The measurement system is sketched in Figure 8.1.

The system was qualified through use of a calibrated granite surface slab that was traceable to the National Bureau of Standards. Repeatability in the positioning system was determined to be .004 mm rms through repeated measurements. The dial indicator was assigned an accuracy of ± 0.013 mm. This was the published calibrated accuracy of the instrument. The uncertainty was then determined to be approximately 0.5 mrad. Measurements were taken every

38 mm on diametrical scans across the facet. Diametrical scans were taken every 45 degrees or 4 scans per facet. Each scan consisted of 17 to 21 points for a total of 73 points per facet. Individual scans were treated independently in the data reduction procedure. The scans were individually compared to an ideal spherical curve having a radius of 2.146 meters. Tilt of the facet during measurement was compensated for by regression about the ideal spherical curve. Typical results are shown in Figure 8.2. The ideal curve is represented by the horizontal line at slope error equal to zero. Typical slope errors for the 300 mm facets were 0.3 to 0.4 mrad rms.

8.2 Measurement of Full-Size Facet Slope Errors

Measurement of slope error in the full-size facets was done in a Cartesian coordinate system. The system consisted of a set of precision compounded slides that provided positioning in the X-Y (horizontal) plane. The X and Y were treated as independent variables, while the Z (vertical) axis was measured by a dial indicator suspended above the facet. The system is sketched in Figure 8.3.

The majority of uncertainty in the system was associated with the dial indicator. Slides were qualified through use of the calibrated granite surface slab. The calibrated accuracy of the dial indicator was .013 mm. Data points were taken at 38 mm intervals to ensure that errors in slope error measurements would be below 0.5 mrad. Repeated measurements on facets gave a repeatability of ± 0.1 mrad rms slope error.

Since the volumetric accuracy of the outside vendor's CMM was twice that of SKI's CMM, the accuracy in the rms slope error was assumed to be twice that of SKI's accuracy. Slope error measurements between the two CMM's were within 10% of one another. The closeness of the results (typically ± 0.05 mrad) indicated that SKI's CMM was well within an accuracy of ± 0.5 mrad.

The CMM system used for the full-size facets was the Sheffield Apollo Cordax RS-50. The volumetric accuracy of this system was .014 mm. However, for the relatively small volume required to measure the facets, a conservative volumetric accuracy of .007 mm (.0003 inch) could be extrapolated from the given specifications. Converted into slope error terms on a 19 mm grid, this would give an uncertainty in slope error measurements of less than 0.4 mrad. The system is shown in Figure 8.4.

Accuracy in slope error measurements was a function of Z-deflection accuracy and grid spacing. Therefore, the same accuracy in slope error could be achieved by reducing the grid spacing by 50%, provided the accuracy in Z-deflection was doubled. This was the case for measurements taken by the outside vendor. However, as mentioned earlier, the overall rms slope error would increase slightly due to the larger data set.

A full-size facet was subsequently exposed to high humidity and remeasured as an indicator of dimensional stability. The facet was placed in an environmental chamber at 100% relative humidity for three days. The facet was measured within a few hours of removal from the chamber. The difference in RMS slope error measurements was .09 mrad; well within the uncertainty of the measurement system.

A similar evaluation as mentioned in the previous paragraph was done for exposure to 90 °C. The facet was placed in an environmental chamber at 90 °C for a period of 4 days. The facet was again measured within hours of removal from the chamber. The difference between RMS slope error measurements was 0.25 mrad.

Results of X-axis and Y-axis slope errors and Z-deflection errors are shown in Figures 8.5, 8.6, and 8.7, respectively. Legends for the circles plotted within the facet outline are given in the upper left corner of each figure. RMS slope errors are separated into the X and Y partial fractions. The total rms slope error of the facet was defined as the root sum square of the X and Y rms errors.

The data reduction computer program used for determining the overall slope error was designed to give the minimized global slope error. The program iterates the translational and rotational axes until a minimum global slope error can be achieved. This technique is referred to as the downhill simplex method. A subroutine taken from Numerical Recipes (Ref. 7) was used to find parameters of a paraboloidal equation that would minimize slope error.

The computer program was tested and qualified by two methods. The first method was reducing CMM data by a much simpler computer program. The simplicity of this program was due to exact positioning of the mold during data acquisition. Therefore, iteration was not required, and a global rms slope error could be determined easily. Then the data was reduced using the computer program that uses the downhill simplex method. The difference between the

results was within 10% of one another. The second method of qualifying the computer program was creating a data file with a theoretical global rms slope error of zero and allowing the program to reduce this data. This would give the error in the results of the program. The results of this test determined that the error within the program was less than 8×10^{-4} mrad.

Slope errors with a period, or characteristic dimension, less than 19 mm (0.75 inches) were termed "local" errors. There were several causes of local slope errors in the facet. The primary cause was dimpling due to coefficient of thermal expansion mismatch and adhesive cure shrinkage. Another cause was due to entrapment of airborne particles between the face sheet and mold during fabrication. This problem was eliminated prior to localized slope error measurements and consequently was not a measurement concern. Therefore, it was decided that if small divots were not optically visible in the facet, no attempts would be made to measure them.

Since dimpling was uniform on the entire surface of any facet, a small section could be measured as a representative section for the entire facet.

Local slope errors were not able to be accurately read by the available coordinate measuring machines. Early in the project, a mechanical contact surface analyzer was used on uncoated samples. Although cumbersome to set up, the unit provided immediate results in graphics form. This provided a prompt means of accurately estimating the slope error due to dimpling. Later, after samples were coated, a laser system developed in Phase I of this work was used for quantifying local slope errors. The laser system was used to avoid scratching the coated surface with the stylus of the surface analyzer.

The mechanical contact surface analyzer consisted of 0.5 mm and 0.02 mm styluses and a traversing unit capable of a 100 mm traverse. The unit is shown in Figure 8.8. The accuracy of the unit was within ± 1.3 microns (5 micro inches). The most significant dimpling was measured to have a depth of 7 - 10 microns (30 - 40 micro inches). This was measured on a sample at ambient temperature after repeated temperature cycles between ambient and above 180 °F. Results of a typical scan are shown in Figure 8.9. The period of the dimple extends across the length of the scan. Data filtering was used to eliminate surface roughness (period of less than 0.25 mm). The effects of surface roughness were included in later specular reflectance measurements.

Depending on the scan location, a dimple could appear to have a period greater than the honeycomb cell width of 3 mm (about .12 inch). This was the case for any scan that was not parallel to the ribbon of the honeycomb core. The extended period of the dimple was due to the stylus traversing through the center of the cell and then along a number of cell walls.

The SKI laser measurement system was constructed to measure coated facets without danger of scratching the surface from mechanical contact surface analyzers. A laser was positioned over the facet, and its beam was aligned to be parallel to the dish axis so that a perfect concentrator would reflect the beam to the dish focal point. A sensor was mounted at the focal point to measure the intensity of the reflected beam. This sensor could be accurately translated in the horizontal plane to locate the position of peak intensity. As the laser is translated above the facet, motion of the reflected beam near the focal point represents slope error, and this motion was recorded with the sensor.

Figure 8.10 is a photograph of the system, and Figure 8.11 describes the parts. A tripod suspended a set of single axis positioning slides mounted perpendicular to one another and inverted a few centimeters above the focal point. The slides provided a means of tracking shifts in the reflected image. An optical receiver was placed under the slides at an angle that would place the receiver near perpendicular to the reflected beam. This aided in locating the peak intensity of the reflected light beam. The optical receiver was used with an extremely sensitive light intensity meter.

In theory, for a perfectly aligned facet, the reflection of any light beam parallel to the axis of the paraboloid should impinge on a single focal point. Slight deviations from this point could be used to determine local slope errors in the facet. However, this requires the facet to be perfectly aligned with the instrument, which is impractical. Therefore, the position of the facet and focal point were adjusted until large translational movements of the laser beam resulted in extremely small shifts in the reflected image at the focal point. Typically, this shift was within 20 mm for any position on the facet. This provided relatively good alignment.

For extremely short translational scans of the laser beam on the facet, it was determined that the displacement of the reflected image would vary less than 3 mm due to misalignment of the facet. Although radical displacement

shifts indicated local slope errors, a gradual shift in the data set would be indicative of facet misalignment. This shift could introduce errors in the data unless the slope errors were regressed about this gradual slope. Since the local slope errors often made it difficult to determine the tendency of the gradual error offset, a longer scan (40 mm) was taken and the gradual curve of the error in the short scan was interpolated from this larger data set. It was determined that the difference between regression about the interpolated slope error curve and regression about the mean slope error of the 20 mm scan was negligible.

Although the honeycomb ribbon had no specific orientation within the facet, the possibility of scanning along the ribbon would tend to bias the slope errors in the perpendicular axis. To minimize this error, several scans were taken at random locations on the facet. The average of the RMS slope errors of these scans was considered to be the representative RMS slope error.

Laser scans were taken only along a line parallel to the X axis, but both the X and Y component of error were recorded. Scans taken in the Y direction gave similar results and support the validity of this approach. Table 8.1 summarizes the measured error for two scans of the same facet. The combined slope error term is defined as the root sum square of the two components. The combined local slope error is representative of the dimpling or honeycomb print-through. Typical values are 0.5 mrad.

The predominant cause of local slope error in the full-size facet was dimpling, or print-through, due to adhesive cure shrinkage and CTE mismatch. Based on this assumption, the period of the local slope error would be approximately the honeycomb cell width, or about 3 mm (.12 inch). Therefore, it would be necessary to have a laser beam diameter significantly smaller than 3 mm in order to resolve slope errors with this period. The actual diameter of the focused laser beam on the facet was approximately 1 mm (.040 inch). Measuring the location of peak intensity of the laser beam reduced the errors associated with beam spread.

An uncertainty analysis for measurement system was done to determine possible errors associated with the local RMS slope error. Possible significant sources of errors were the rocking, or tilt, of the CDM and laser during the scan, the accuracy and repeatability of the optical receiver, and the regression technique for reducing the data. Error due to rocking of the CDM and laser during the scan was determined by correlating the CDM digital display with the

shift in the light beam image approximately 1.75 meters below. Rocking errors were less than .04 mrad. The induced error in the local slope error would be less than .02 mrad.

The repeatability of the optical receiver was estimated by repeated measurement of the location of a stationary beam. This indicated a repeatability of 0.15 mm. The effect that this error would have on the total RMS local slope error was determined by repeating scans at the same location on the facet and comparing total RMS slope error. A graph of two individual scans taken at the same location is shown in Figure 8.12. The difference in RMS values for these two scans was less than 0.01 mrad. Note that the location of individual honeycomb cells is not apparent because the path of the scan is skewed to the direction of cell rows.

Based on the data results attained from CMM measurement of the facet (#9), a global slope error (measured on a 19 mm Cartesian grid) was 0.55 mrad (rms). These measurements were done prior to coating the facet. Measurements on other facets have shown no more than .25 mrad change due to the process used to apply the coating, thus, giving a maximum global slope error of 0.80 mrad.

Measurement of slope errors within a 19 mm scan showed a local slope error of 0.49 mrad (rms). Total slope error for the final facet was defined as the root sum square of the two values (0.80 and 0.49 mrad), or 0.94 mrad (rms).

Repeatability of the fabrication process was demonstrated by the low slope error of each facet. Fifteen facets were fabricated during this project. None exceeded 0.75 mrad as measured on a 1.5 inch grid pattern prior to being coated.

9.0 Discussion of Results

SKI's objective was to develop a fabrication method for high quality facets and to produce a prototype facet. This work was successfully completed. The facets made during this effort had very accurate contours and high specular reflectance. They also passed numerous tests demonstrating their stability and longevity.

Fifteen facets were assembled as part of this effort. The contour of each facet was within 0.75 mrad of a perfect parabola (all values are reported as one standard deviation unless otherwise noted). Honeycomb print-through (a large source of error for many solar concentrators) was measured to be less than 0.5 mrad. The small amount of dimpling is a result of the dimensional stability of the metal itself and of the adhesive used to join the face sheets to the core. Joint strength was not sacrificed to accomplish this. When the facets were tested in bending, the face sheets would buckle or rupture prior to the adhesive bond failing. The total slope error from print-through and panel contour for the final facet was 0.94 mrad.

The face sheet surface was leveled with a polyimide coating to provide a smooth substrate for the aluminum reflective film. Aluminum oxide was used as a protective film. A specular reflectance of 88% was achieved for a wavelength range of 250-2500 nm and 300-900 nm. This integrated reflectance value is indicative of the optical quality of the facet that was developed in this fabrication technique. Five (5) facets were fabricated with optical films. A few of the facets sustained damage to the optical surface. The optical films and the polyimide leveling coating was removed by chemical stripping. The leveling coat was stripped with a mild acid that slightly increased the surface roughness of the aluminum facet sheet. It is believed that this increased the roughness of the leveled surface. This caused an increase in diffuse reflectance. The thin leveling coat did not cover the increased surface roughness. The significance of this is small because repeated coatings and stripping is unique to the development of the panel fabrication process and will not be done during production.

Although many of the coated facets were durable and could withstand handling and environmental testing, some could not. The coating of one facet was destroyed while the facet was being trimmed. The adhesion between the thin film aluminum and the polyimide coating for this facet was poor. Other facets had excellent adhesion. More work is required to make the coating process more repeatable.

Particulate contamination of the leveling coat was reduced during this effort by improvements to the cleanliness of the work area. Particles now cause only one or two imperfections per facet. Further equipment upgrades will likely reduce this value to near zero.

Testing and analysis of the facets show that they will be dimensionally stable during operation, and no results indicated a short life span. A mathematical model of the facet was subjected to the transient thermal environment of low earth orbit. Although the mean temperature of the facet cycled, the temperature difference between the front and back skin remained small (less than 0.5 °C), and the corresponding distortions of the panel were also small (less than one milliradian). Performance degradation with time was assessed by exposing a facet to 93 °C for four days at 100% relative humidity for over three days. No change in facet shape was measured. The small residual stresses in the facet caused no measurable relaxation or distortion in the part. Panel strength was measured after subjecting a facet to over 4000 cycles in temperatures from 37 to 90 °C and another facet to 25 cycles in relative humidity from room conditions to 100%. The aluminum face sheets failed before the adhesive joint on each facet.

An assembled facet is shown in Figure 9.1 mounted in a wooden display case.

10.0 Summary of Results

Solar Kinetics, Inc. (SKI) has developed a fabrication technique and demonstrated an accurate and durable solar concentrator facet for solar dynamic space systems. The facet is a section of a parabolic concentrator which focuses solar energy to a receiver of a heat engine where it is converted to electricity. Solar dynamic concentrators for space application can be 7 m in diameter. The facet developed by SKI is part of a NASA/Lewis concentrator R&D program. The concentrator is a parabolic axisymmetric dish two meters in diameter with a one meter focal length. The facet is one of 16 identical radial petals that make up the mirrored surface.

The conversion efficiency of solar dynamic systems is a strong function of the quality of the concentrator. The facets are required to have small contour (slope) errors and a smooth optical surface to minimize the diffusion of the reflected energy. The facets must also have high specular reflectivity and must be stable in environment of low earth orbit.

The objective of this work was to develop a fabrication method for high quality facets and to produce a prototype facet. The objective was met. Key accomplishments include the following:

- * Facet slope error less than one milliradian,
- * Repeatability of facet assembly,
- * Minimal honeycomb print-through,
- * High specular reflectivity (88%),
- * Dimensional stability and strength maintained through accelerated testing.

Appendix A
Computer Program for Facet Contour Data Reduction


```

10 REM*****
20 REM
30 REM          PROGRAM "SPHERE" (6/20/90).
40 REM  COMPUTES SLOPE AND DISPLACEMENT ERRORS FOR 12X12 SPHERICAL
50 REM  FACET. (MEASUREMENTS TAKEN IN R,0,Z COORDINATE SYSTEM.)
60 REM  DETERMINES MOUNTED POSITION OF FACET BY MINIMIZING SUM
70 REM  OF SQUARES OF SLOPE ERRORS. USES SECANT METHOD TO FIND
80 REM  R-COORDINATE OF CENTER OF CIRCLE WHICH MAKES DERIVATIVE
90 REM  OF SUM OF SQUARES ZERO. NOTE: THIS PROGRAM REMOVES TILT
94 REM  OF THE FACET ONLY ABOUT AN AXIS PERPENDICULAR TO THE
96 REM  DIRECTION OF THE SCAN.
100 REM
110 REM          VARIABLE DEFINITIONS
120 REM
130 REM  RAD: RADIUS OF SPHERICAL FACET
140 REM  THETA: ANGLE OF SCAN
150 REM  N: NUMBER OF DATA POINTS IN SCAN
160 REM  R0,Z0: COORDINATES OF CENTER OF FACET
170 REM  R(I),Z(I): COORDINATES OF THE ITH DATA POINT
180 REM  SMEAS(I): MEASURED SLOPE BETWEEN R(I) AND R(I+2)
190 REM  AVG(I): AVERAGE OF R(I) AND R(I+2)
200 REM  A,B: THEORETICAL COORDINATES OF CENTER OF CIRCLE DEFINED BY SCAN
210 REM  APAST: PREVIOUS VALUE OF A IN SECANT METHOD
220 REM  APRES: PRESENT VALUE OF A IN SECANT METHOD
230 REM  DERIV1: PREVIOUS VALUE OF DERIVATIVE IN SECANT METHOD
240 REM  DERIV2: PRESENT VALUE OF DERIVATIVE IN SECANT MEHTOD
250 REM  SLPERR(I): SLOPE ERROR AT AVG(I)
260 REM  DISERR(I): DISPLACEMENT ERROR AT R(I)
270 REM  RMSS: RMS SLOPE ERROR
280 REM  RMSD: RMS DISPLACEMENT ERROR
290 REM  DUM1:  *          *
300 REM  DUM2:  *          DUMMY          *
310 REM  U:    *          VARIABLES      *
320 REM  W:    *          *
330 REM
340 REM*****
350 REM
360 REM  DECLARATION
370 REM
380 REM*****
390 CLEAR
400 CLS
410 DEFDBL A-H,O-Z
420 DEFINT I-N
430 DIM R(25),Z(25),SMEAS(25),AVG(25),SLPERR(25),DISERR(25)
440 REM*****
450 REM
460 REM  INPUT AND ECHO PRINT DATA. CORRECT DATA POINTS SO
470 REM  THAT POINT AT CENTER OF FACET IS (0,0).
480 REM
490 REM  NOTE: DATA MUST BE ENTERED IN ORDER, WITH LEAST(MOST
500 REM        NEGATIVE) R FIRST. ENTER A DATA POINT LIKE THIS:
510 REM        "R,Z".
520 REM
530 REM*****
535 PRINT "NOTE: DATA IN INPUT FILE SHOULD BE ENTERED IN ASCENDING ORDER

```

```

536 PRINT "          WITH RESPECT TO R. DO NOT LEAVE A BLANK LINE BETWEEN
537 PRINT "          THE LAST DATA PAIR AND END OF FILE."
538 PRINT
540 INPUT "FILE TO READ FROM (INCLUDING EXTENTION)";INFILE$
550 INPUT "FILE TO WRITE TO (INCLUDING EXTENTION)";OUTFILE$
560 OPEN "I",#1,INFILE$
570 N=1
580 WHILE NOT EOF(1)
590     INPUT# 1,R(N),Z(N)
600     N=N+1
610 WEND
620 N=N-1
630 CLOSE# 1
640 INPUT "RADIUS OF SPHERICAL FACET";RAD
650 INPUT "ANGLE OF SCAN"; THETA
670 INPUT "R,Z COORDINATES OF CENTER OF FACET";R0,Z0
680 PRINT "YOU INPUT THE FOLLOWING DATA:"
690 PRINT "RADIUS:",RAD
700 PRINT "ANGLE OF SCAN:",THETA
710 PRINT N,"CORRECTED R,Z POINTS:"
720 FOR I=1 TO N
730     R(I)=R(I)-R0 : Z(I)=Z(I)-Z0
740     PRINT R(I),Z(I)
750 NEXT I
760 REM*****
770 REM
780 REM  COMPUTE MEASURED SLOPE AND AVERAGE R BETWEEN EVERY OTHER
790 REM  DATA POINT. FIND SMALLEST Z AND USE CORRESPONDING R AS
800 REM  INITIAL GUESS OF ROOT FOR SECANT METHOD.
810 REM
820 REM*****
830 FOR I=1 TO N-2
840     SMEAS(I)=(Z(I+2)-Z(I))/(R(I+2)-R(I))
850     AVG(I)=(R(I)+R(I+2))/2.0
860 NEXT I
870 REM
880 SMALLZ=Z(1) : A=R(1)
890 FOR I=1 TO N
900     IF Z(I)<SMALLZ THEN
902         SMALLZ=Z(I)
904         A=Z(I)
906     END IF
910 NEXT I
920 REM*****
930 REM
940 REM  DETERMINE VALUE OF A WHICH MAKES DERIVATIVE OF SUM OF
950 REM  SQUARES ZERO. APPLY SECANT METHOD UNTIL THE DERIVATIVE
960 REM  IS PRACTICALLY ZERO.
970 REM
980 REM*****
990 APAST=A : APRES=A+1.0#
1000 ICALL=1 : ISTOP=0
1010 GOSUB 1450
1020 DERIV1=SUM
1030 IF ABS(DERIV1)<1D-12 THEN GOTO 1180
1040 A=APRES

```

```

1050 GOSUB 1450
1060 DERIV2=SUM
1070 WHILE ISTOP=0
1080     A=APRES-DERIV2*(APAST-APRES)/(DERIV1-DERIV2)
1090     DERIV1=DERIV2
1100     APAST=APRES
1110     APRES=A
1120     GOSUB 1450
1130     DERIV2=SUM
1140     PRINT "ESTIMATE OF ROOT","DERIVATIVE"
1150     PRINT A,DERIV2
1160     IF ABS(DERIV2)<1D-12 THEN ISTOP=1
1170 WEND
1180 REM*****
1190 REM
1200 REM  OUTPUT SLOPE ERRORS (MRAD) AND DISPLACEMENT ERRORS (IN.).
1210 REM
1220 REM*****
1230 PRINT "THE ROOT OF DERIVATIVE IS",A
1240 ICALL=2
1250 GOSUB 1450
1260 PRINT "WHICH GIVES AN RMS SLOPE ERROR OF",RMSS
1270 GOSUB 1690
1280 PRINT "AND AN RMS DISPLACEMENT ERROR OF",RMSD
1290 OPEN "O",#1,OUTFILE$
1300 WRITE# 1, "THETA:",THETA
1310 WRITE# 1, "INPUT RADIUS:",RAD
1320 WRITE# 1, "R","SLOPE ERROR"
1330 FOR I=1 TO N-2
1340     WRITE# 1, AVG(I),SLPERR(I)
1350 NEXT I
1360 WRITE# 1, "RMS:",RMSS
1370 WRITE# 1,
1380 WRITE# 1, "R","DISPLACEMENT ERROR"
1390 FOR I=1 TO N
1400     WRITE# 1, R(I),DISERR(I)
1410 NEXT I
1420 WRITE# 1, "RMS:",RMSD
1430 CLOSE# 1
1440 END
1450 REM*****
1460 REM
1470 REM  SUBROUTINE TO COMPUTE DERIVATIVE OF SUM OF SQUARES
1480 REM  OF SLOPE ERRORS (IF ICALL=1) OR TO COMPUTE SLOPE
1490 REM  ERRORS (IF ICALL=2). SLOPE ERRORS ARE OUTPUT AS
1495 REM  POS. (+) IF SLOPE IS TOO STEEP.
1500 REM
1510 REM*****
1520 REM
1530 SUM=0.0 : RMSS=0.0
1540 FOR J=1 TO N-2
1550     DUM1=AVG(J)-A
1560     DUM2=(RAD^2-DUM1^2)^(0.5)
1570     IF ICALL=1 THEN
1580         U=SMEAS(J)-DUM1/DUM2
1590         W=U*(1/DUM2+DUM1^2*(1/DUM2)^3)

```

```

1600     SUM=SUM+W
1604     END IF
1610     IF ICALL=2 THEN
1620         SLPERR(J)=(ATN(SMEAS(J))-ATN(DUM1/DUM2))*1000.0
1625         IF R(J)<0.0 THEN SLPERR(J)=-SLPERR(J)
1630         RMSS=RMSS+SLPERR(J)^2
1634     END IF
1640     DUM1=0.0 : DUM2=0.0
1650 NEXT J
1660 IF ICALL=2 THEN RMSS=(RMSS/(N-2))^(0.5)
1670 REM END OF SUBROUTINE
1680 RETURN
1690 REM*****
1700 REM
1710 REM  SUBROUTINE TO COMPUTE DISPLACEMENT ERRORS.  FIRST
1720 REM  COMPUTE B FROM VALUE OF A FOUND EARLIER.
1730 REM
1740 REM*****
1750 REM
1760 B=(RAD^2-A^2)^(0.5)
1770 RMSD=0.0
1780 FOR K=1 TO N
1790     DISERR(K)=Z(K)-(-(RAD^2-(R(K)-A)^2)^(0.5)+B)
1800     RMSD=RMSD+DISERR(K)^2
1810 NEXT K
1820 RMSD=(RMSD/N)^(0.5)
1830 REM END OF SUBROUTINE
1840 RETURN

```



```

'*****
' *
' *           Program "PARABOLA" (7/90)
' *           Written and Compiled in Turbo Basic
' *
' * Computes slope error of parabolic panel measured in x,y,z
' * coordinates. Nominal spacing between x's and y's must be constant.
' * Finds translation and rotation parameters in general equation of
' * paraboloid which minimize rms slope error. Finds parameters by
' * downhill simplex method due to Nelder and Mead (1965). Input file
' * required. Input file should only have x,y,z data points in this
' * format:
' *           "x,y,z"
' *           "x,y,z"
' *           "x,y,z"....
' * The data points may be in any order as long as there are no
' * blank lines between data points or after the final data point.
' *
' * Input: * measured x,y,z coordinates.
' *        * focal length of panel
' *        * initial guesses for 4 parameters
' *
' * Output: * x and y slope errors between measured points
' *         * z error at measured points
' *         * rms slope and rms z errors
' *         * value of 4 iteration parameters and slope error after
' *         each iteration
' *
' * Variable Definitions:
' *
' * ID$: string which identifies facet being analyzed
' * FOCAL: focal length of paraboloid
' * DELTA: nominal distance between measured x and y points
' * AXIS$: axis which facet is aligned with (either x or y)
' * A: x coordinate of the vertex of the paraboloid
' * B: y coordinate of the vertex of the paraboloid
' * C: z coordinate of the vertex of the paraboloid (only used
' *    to calculate displacement errors)
' * PSI,THETA: Euler angles in paraboloidal equation (not
' *            rotations about x or y axes)
' * X: measured x coordinate
' * Y: measured y coordinate
' * Z: measured z coordinate
' * ZIDEAL: ideal value of z computed from paraboloidal equation
' * ACTUAL: measured slope between two data points
' * THEORET: theoretical slope between two data points
' * NUMPTS: number of x,y,z data points
' * NUMXERS: number of x slope error terms
' * NUMYERS: number of y slope error terms
' * IX,JX: indices of data points used to calculate x slope error
' * IY,JY: indices of data points used to calculate y slope error
' * RMSS: rms combined x-y slope error
' * RMSXS: rms x slope error
' * RMSYS: rms y slope error
' * RMSD: rms displacement error
' * XSLPER: x slope error between two measured points

```

```

'* YSLPER: y slope error between two measured points (note
'*         that no two x,y points will have both an x slope error
'*         and a y slope error between them)
'* DISER: displacement error at a measured data point
'* U: *           *
'* V: *   dummy   *
'* W: *   variables *
'* M: *           *
'* L: *           *
'*     The following variables are defined in the book "Numerical
'* Recipes" by William H. Press, et al., page 292, from which part
'* of this program is taken. Changes in notation are indicated.
'*     P
'*     Q (in this program) = Y (in the book)
'*     ALPHA, BETA, GAMMA
'*     NDIM, MPTS
'*
'*****
CLEAR : CLS
DEFDBL A-H,O-Z : DEFINT I-N
'
' 4 iteration variables; 5 vertices of simplex
'
NDIM=4 : MPTS=5
'
DIM X(600),Y(600),Z(600),ZIDEAL(600)
DIM P(MPTS,NDIM),Q(MPTS),PR(NDIM),PRR(NDIM),PBAR(NDIM)
DIM DISER(600),XSLPER(1200),YSLPER(1200)
DIM IX(1200),JX(1200),IY(1200),JY(1200)
'*****
'*
'* Input and echo print measurement info from terminal.
'*
'*****
INPUT "IDENTIFICATION OF FACET";ID$
INPUT "COMMENTS";COMMENTS$
INPUT "FOCAL LENGTH";FOCAL
INPUT "NOMINAL DISTANCE BETWEEN X'S AND Y'S";DELTA
INPUT "RADIAL AXIS OF FACET ALIGNED WITH X OR Y AXIS (X/Y)";AXIS$
INPUT "NAME OF INPUT FILE (INCLUDING EXTENTION)";INFILE$
PRINT : PRINT "INITIAL GUESS VERTEX (4 PARAMETERS):" : PRINT
PRINT "NOTE: A,B ARE THE X,Y COORDINATES OF THE VERTEX OF THE"
PRINT "      PARABOLOID. PSI AND THETA ARE 2 OF THE 3 EULER ANGLES."
PRINT "      (PSI AND THETA ARE NOT ROTATIONS ABOUT THE X AND Y AXES."
PRINT "      FOR THE DEFINITIONS OF EULER'S ANGLES, SEE ANY ADVANCED"
PRINT "      DYNAMICS BOOK.) THE Z TRANSLATOR AND THE THIRD EULER"
PRINT "      ANGLE ARE NOT REQUIRED TO CALULATE SLOPE ERROR." : PRINT
INPUT "A, B, PSI(DEG), THETA(DEG)";P(1,1),P(1,2),P(1,3),P(1,4)
CLS : PRINT "YOU ENTERED THE FOLLOWING INFORMATION" : PRINT
PRINT "FACET: ";ID$
PRINT "COMMENTS: ";COMMENTS$
PRINT "FOCAL LENGTH: ";FOCAL
PRINT "X,Y INCREMENT LENGTH: ";DELTA
PRINT "FACET ALIGNED WITH ";AXIS$;" AXIS"
PRINT "INPUT FILE: ";INFILE$
PRINT "INITIAL GUESSES FOR A,B,PSI,THETA :"

```

```

PRINT P(1,1),P(1,2),P(1,3),P(1,4)
PRINT "PRESS <ENTER> TO CONTINUE" : INPUT DUMMY$
/*****
/*
/* Input x,y,z data points from input file. Find the pairs
/* of points that can be used to compute slope errors.
/*
/*****
CLS
PRINT "READING RAW DATA AND PREPARING FOR ITERATION. PLEASE WAIT."
OPEN "I",#1,INFILE$
NUMPTS=0
WHILE NOT EOF(1)
  NUMPTS=NUMPTS+1
  INPUT# 1,X(NUMPTS),Y(NUMPTS),Z(NUMPTS)
WEND
/
/ Determine the indices of pairs of points which can be used
/ to compute x and y slope errors. Also determine the number
/ of x and y slope error terms.
/
NUMXERS=0: NUMYERS=0
/
FOR I=1 TO NUMPTS
  FOR J=1 TO NUMPTS
  /
  / For x slope errors, find indices of adjacent points having
  / the same y-coordinate.
  /
  IF ABS(X(J)-X(I)-DELTA) < .05 AND ABS(Y(J)-Y(I)) < .05 THEN
    NUMXERS=NUMXERS+1
    IX(NUMXERS)=I
    JX(NUMXERS)=J
  END IF
  /
  / For y slope errors, find indices of adjacent points having
  / the same x-coordinate.
  /
  IF ABS(Y(J)-Y(I)-DELTA) < .05 AND ABS(X(J)-X(I)) < .05 THEN
    NUMYERS=NUMYERS+1
    IY(NUMYERS)=I
    JY(NUMYERS)=J
  END IF
  /
  NEXT J
NEXT I
/
PRINT : PRINT NUMPTS;"X,Y,Z POINTS WERE READ FROM THE INPUT FILE"
PRINT : PRINT "THERE WILL BE";NUMXERS+NUMYERS;"SLOPE ERROR TERMS"
PRINT
PRINT "NOTE: THIS PROGRAM MAY REQUIRE AS MANY AS 1000 ITERATIONS"
PRINT " (ABOUT 30 MINUTES) TO CONVERGE TO A MINIMUM. THE PROGRAM"
PRINT " SHOULD ALWAYS BE RUN SEVERAL TIMES WITH VARYING INITIAL"
PRINT " GUESSES AND THE RESULTS COMPARED TO ENSURE THAT THE GLOBAL"
PRINT " MINIMUM HAS BEEN FOUND. IF EACH OF THE 4 PARAMETERS IN THE"
PRINT " INITIAL GUESS IS WITHIN 5 INCHES/DEGREES OF ITS ACTUAL"

```

```

PRINT "          VALUE, THE PROGRAM SHOULD CONVERGE TO THE GLOBAL MINIMUM."
PRINT
PRINT "PRESS <ENTER> TO CONTINUE" : INPUT DUMMY$
CLOSE# 1
/*****
/*
/* Start iteration procedure.
/*
/*****
CLS : PRINT "BEGINNING ITERATION PROCEDURE"
/
/ Form other 4 vertices of simplex from initial guess vertex
/
FOR I=2 TO MPTS
  FOR J=1 TO NDIM
    P(I,J)=P(1,J)
    IF I=J+1 THEN P(I,J)=P(1,J)+2.0
  NEXT J
NEXT I
/
/ Evaluate slope error at each of the 5 initial vertices
/
FOR I=1 TO MPTS
  A=P(I,1) : B=P(I,2) : PSI=P(I,3) : THETA=P(I,4)
  GOSUB 400
  Q(I)=RMSS
NEXT I
/
/ Branch to iteration subroutine.
/
GOSUB 100
/
/ Iteration complete.
/
/*****
/*
/* Compute slope and displacement errors from parameters found by
/* iteration. Send slope error and displacement error results to
/* output file.
/*
/*****
/
/ Branch to slope error subroutine
/
A=P(ILO,1) : B=P(ILO,2) : PSI=P(ILO,3) : THETA=P(ILO,4)
GOSUB 400
/
/ Branch to displacement error subroutine
/
GOSUB 500
/
CLS
PRINT "FACET: ";ID$
PRINT "COMMENTS: ";COMMENT$ : PRINT
PRINT "***** ITERATION RESULTS *****" : PRINT
PRINT "NUMBER OF DATA POINTS: ";NUMPTS

```

```

PRINT "NUMBER OF X SLOPE ERRORS: ";NUMXERS
PRINT "NUMBER OF Y SLOPE ERRORS: ";NUMYERS
PRINT "NUMBER OF ITERATIONS: ";ITER : PRINT
PRINT "FINAL ITERATION PARAMETERS:"
PRINT "A= ";A
PRINT "B= ";B
PRINT "PSI= ";PSI*(180.0/(4*ATN(1))); " DEG"
PRINT "THETA= ";THETA*(180.0/(4*ATN(1))); " DEG" : PRINT
PRINT "ERRORS:"
PRINT "X SLOPE ERROR= ";RMSXS;" MRAD"
PRINT "Y SLOPE ERROR= ";RMSYS;" MRAD"
PRINT "COMBINED X-Y SLOPE ERROR= ";RMSS;" MRAD"
PRINT "DISPLACEMENT ERROR= ";RMSD : PRINT
INPUT "SEND RESULTS TO OUTPUT FILE (Y/N)";A$
,
IF A$="Y" OR A$="y" THEN
  INPUT "NAME OF OUTPUT FILE (INCLUDING EXTENTION)";OUTFILE$
  OPEN "O",#2,OUTFILE$
  WRITE# 2,"FACET:",ID$
  WRITE# 2,"FOC LGTH=",FOCAL
  WRITE# 2,"X","Y","XSERR(MR) ","YSERR(MR) "
  ,
  FOR I=1 TO NUMXERS
    L=IX(I) : M=JX(I)
    WRITE# 2,(X(M)+X(L))/2.0,Y(M),XSLPER(I),"*****"
  NEXT I
  ,
  FOR I=1 TO NUMYERS
    L=IY(I) : M=JY(I)
    WRITE# 2,X(M),(Y(M)+Y(L))/2.0,"*****",YSLPER(I)
  NEXT I
  ,
  WRITE# 2,
  WRITE# 2,"RMSXSERR=",RMSXS,"MR"
  WRITE# 2,"RMSYSERR=",RMSYS,"MR"
  WRITE# 2,"RMS(X&Y)=",RMSS,"MR"
  WRITE# 2,
  WRITE# 2,"X","Y","DISPLERR"
  ,
  FOR I=1 TO NUMPTS
    WRITE# 2,X(I),Y(I),DISER(I)
  NEXT I
  ,
  WRITE# 2,
  WRITE# 2,"RMSDISER=",RMSD
  CLOSE# 2
  ,
END IF
,
INPUT "PLOT RESULTS ON SCREEN (Y/N)";PLOT$
IF PLOT$="Y" OR PLOT$="y" THEN GOSUB 600 ' go to plotting subroutine
,
50 SCREEN 0 : CLS
INPUT "REDRAW PLOTS WITH NEW SCALE (Y/N)";REDRAW$
IF REDRAW$="Y" OR REDRAW$="y" THEN
  OPEN "I",#1,INFILE$

```

```

FOR I=1 TO NUMPTS
  INPUT# 1,X(I),Y(I),Z(I)
NEXT I
CLOSE# 1
A=P(ILO,1) : B=P(ILO,2) : PSI=P(ILO,3) : THETA=P(ILO,4)
GOSUB 400
GOSUB 500
GOSUB 600
GOTO 50
END IF
'
END
100 '*****
' *
' * Subroutine "AMOEBA". Taken from the book "Numerical Recipes",
' * by William H. Press, et al., page 292. Iterates to find
' * parameters of paraboloidal equation which minimize slope error.
' *
'*****
ALPHA=1.0 : BETA=0.5 : GAMMA=2.0
ITER=0
200 ILO=1
IF Q(1) > Q(2) THEN
  IHI=1
  INHI=2
ELSE
  IHI=2
  INHI=1
END IF
FOR I=1 TO MPTS
  IF Q(I) < Q(ILO) THEN ILO=I
  IF Q(I) > Q(IHI) THEN
    INHI=IHI
    IHI=I
  ELSEIF Q(I) > Q(INHI) THEN
    IF I <> IHI THEN INHI=I
  END IF
NEXT I
IF ITER > 0 THEN
  PRINT "RMS SLOPE ERROR=",Q(IHI),"MRAD"
END IF
RTOL=2.0*ABS(Q(IHI)-Q(ILO))/(ABS(Q(IHI))+ABS(Q(ILO)))
IF RTOL < 1D-14 OR QPAST=Q(IHI) THEN GOTO 300
QPAST=Q(IHI)
IF ITER >= 1000 THEN
  PRINT : PRINT "EXCEEDING MAXIMUM ITERATIONS. CHECK FOR CONVERGENCE."
END IF
ITER=ITER+1
FOR J=1 TO NDIM
  PBAR(J)=0.0
NEXT J
FOR I=1 TO MPTS
  IF I <> IHI THEN
    FOR J=1 TO NDIM
      PBAR(J)=PBAR(J)+P(I,J)
    NEXT J

```

```

END IF
NEXT I
FOR J=1 TO NDIM
  PBAR(J)=PBAR(J)/NDIM
  PR(J)=(1.0+ALPHA)*PBAR(J)-ALPHA*P(IHI,J)
NEXT J
A=PR(1) : B=PR(2) : PSI=PR(3) : THETA=PR(4)
GOSUB 400
QPR=RMSS
IF QPR <= Q(ILO) THEN
  FOR J=1 TO NDIM
    PRR(J)=GAMMA*PR(J)+(1.0-GAMMA)*PBAR(J)
  NEXT J
  A=PRR(1) : B=PRR(2) : PSI=PRR(3) : THETA=PRR(4)
  GOSUB 400
  QPRR=RMSS
  IF QPRR < Q(ILO) THEN
    FOR J=1 TO NDIM
      P(IHI,J)=PRR(J)
    NEXT J
    Q(IHI)=QPRR
  ELSE
    FOR J=1 TO NDIM
      P(IHI,J)=PR(J)
    NEXT J
    Q(IHI)=QPR
  END IF
ELSEIF QPR >= Q(INHI) THEN
  IF QPR < Q(IHI) THEN
    FOR J=1 TO NDIM
      P(IHI,J)=PR(J)
    NEXT J
    Q(IHI)=QPR
  END IF
  FOR J=1 TO NDIM
    PRR(J)=BETA*P(IHI,J)+(1.0-BETA)*PBAR(J)
  NEXT J
  A=PRR(1) : B=PRR(2) : PSI=PRR(3) : THETA=PRR(4)
  GOSUB 400
  QPRR=RMSS
  IF QPRR < Q(IHI) THEN
    FOR J=1 TO NDIM
      P(IHI,J)=PRR(J)
    NEXT J
    Q(IHI)=QPRR
  ELSE
    FOR I=1 TO MPTS
      IF I <> ILO THEN
        FOR J=1 TO NDIM
          PR(J)=0.5*(P(I,J)+P(ILO,J))
          P(I,J)=PR(J)
        NEXT J
        A=PR(1) : B=PR(2) : PSI=PR(3) : THETA=PR(4)
        GOSUB 400
        Q(I)=RMSS
      END IF
    END IF

```

```

        NEXT I
    END IF
ELSE
    FOR J=1 TO NDIM
        P(IHI,J)=PR(J)
    NEXT J
    Q(IHI)=QPR
END IF
CLS
PRINT "ITERATION:";ITER : PRINT
PRINT "A=",P(IHI,1)
PRINT "B=",P(IHI,2)
PRINT "PSI=",P(IHI,3),"DEG"
PRINT "THETA=",P(IHI,4),"DEG" : PRINT
GOTO 200
300 RETURN
400 /*****
    *
    * Subroutine to compute slope errors.
    *
    *****/
PSI=PSI*((4*ATN(1))/180.0)
THETA=THETA*((4*ATN(1))/180.0) 'degrees to radians
/
/ Compute z(ideal) from general equation of paraboloid
/
FOR K=1 TO NUMPTS
    U=SIN(THETA)^2
    V1=SIN(2*THETA)*((Y(K)-B)*COS(PSI)-(X(K)-A)*SIN(PSI))
    V2=-4*FOCAL*COS(THETA)
    V=V1+V2
    W1=-4*FOCAL*SIN(THETA)*((X(K)-A)*SIN(PSI)-(Y(K)-B)*COS(PSI))
    W2=(X(K)-A)^2*(COS(PSI)^2+COS(THETA)^2*SIN(PSI)^2)
    W3=(Y(K)-B)^2*(SIN(PSI)^2+COS(THETA)^2*COS(PSI)^2)
    W4=(X(K)-A)*(Y(K)-B)*SIN(2*PSI)*SIN(THETA)^2
    W=W1+W2+W3+W4
/
/ Stop program if it attempts to take square root of negative
/ number or divide by zero.
/
IF V^2-4*U*W < 0.0 OR SIN(THETA)=0.0 THEN
    PRINT "A=",A
    PRINT "B=",B
    PRINT "PSI=",PSI*(180.0/(4*ATN(1)))
    PRINT "THETA=",THETA*(180.0/(4*ATN(1)))
    PRINT
    PRINT " THESE ARE THE CURRENT PARAMETERS IN THE ITERATION."
    PRINT " PARABOLOIDAL EQUATION HAS NO SOLUTION FOR THESE VALUES."
    PRINT " RE-START PROGRAM WITH NEW INITIAL GUESS VERTEX."
    STOP
END IF
/
ZIDEAL(K)=(-V-(V^2-4*U*W)^0.5)/(2*U) 'paraboloidal equation
/
NEXT K
/

```



```

XSUM=0.0 : YSUM=0.0
'
' Loop to compute x slope errors
'
FOR K=1 TO NUMXERS
  L=IX(K) : M=JX(K)
  ACTUAL=ATN((Z(M)-Z(L))/(X(M)-X(L)))
  THEORET=ATN((ZIDEAL(M)-ZIDEAL(L))/(X(M)-X(L)))
  XSLPER(K)=(ACTUAL-THEORET)*1000.0 ' rad to mrad
  IF THEORET < 0 THEN XSLPER(K)= -XSLPER(K) ' sign convention
  XSUM=XSUM+XSLPER(K)^2
NEXT K
'
' Loop to compute y slope errors
'
FOR K=1 TO NUMYERS
  L=IY(K) : M=JY(K)
  ACTUAL=ATN((Z(M)-Z(L))/(Y(M)-Y(L)))
  THEORET=ATN((ZIDEAL(M)-ZIDEAL(L))/(Y(M)-Y(L)))
  YSLPER(K)=(ACTUAL-THEORET)*1000.0 ' rad to mrad
  IF THEORET < 0 THEN YSLPER(K)= -YSLPER(K) ' sign convention
  YSUM=YSUM+YSLPER(K)^2
NEXT K
'
RMSXS=(XSUM/NUMXERS)^0.5
RMSYS=(YSUM/NUMYERS)^0.5
RMSS=(RMSXS^2+RMSYS^2)^0.5
'
RETURN
500 '*****
' *
' * Subroutine to compute displacement errors.
' *
' *****
'
' Find coordinates X(LOWI),Y(LOWI) of lowest Z.
'
SMALLZ=Z(1) : LOWI=1
FOR I=2 TO NUMPTS
  IF Z(I) < SMALLZ THEN
    SMALLZ=Z(I)
    LOWI=I
  END IF
NEXT I
'
' Find C by requiring that Z(LOWI)=ZIDEAL(LOWI) at X(LOWI),Y(LOWI).
' (Use Z(LOWI) as a reference point for the other z's.)
'
C=Z(LOWI)-ZIDEAL(LOWI)
'
' Compute displacement errors.
'
DISSUM=0.0
FOR I=1 TO NUMPTS
  DISER(I)=Z(I)-(ZIDEAL(I)+C)
  DISSUM=DISSUM+DISER(I)^2

```

```

NEXT I
RMSD=(DISSUM/NUMPTS)^0.5
RETURN
600 /*****
/*
/* Subroutine to plot results on screen.
/*
*****/
CLS
PRINT " AFTER EACH PLOT IS DISPLAYED, PRESS <PRINT SCREEN> TO PRINT"
PRINT "THE PLOT. ONCE THE PLOT HAS BEEN PRINTED, PRESS <ENTER> TO"
PRINT "ADVANCE TO THE NEXT PLOT OR TO THE END OF THE PROGRAM." : PRINT
/
/ Scale errors for plotting. Transform x's and y's using final iteratio
/ parameters.
/
PRINT "SCALE FOR X ERRORS,Y ERRORS,Z ERRORS (3 NUMBERS)"
INPUT XSCALE,YSCALE,ZSCALE
INPUT "PRESS <ENTER> TO DISPLAY THE FIRST PLOT.",DUMMY$
FOR I=1 TO NUMPTS
  XSLPER(I)=(XSLPER(I)/XSCALE)*0.75
  YSLPER(I)=(YSLPER(I)/YSCALE)*0.75
  DISER(I)=(DISER(I)/ZSCALE)*0.75
  XTRANS=(X(I)-A)*COS(PHI)+(Y(I)-B)*SIN(PHI)
  XCOMP=-COS(THETA)*SIN(PHI)
  YCOMP=COS(THETA)*COS(PHI)
  Y(I)=(X(I)-A)*XCOMP+(Y(I)-B)*YCOMP+(Z(I)-C)*SIN(THETA)
  X(I)=XTRANS
NEXT I
/
/ If facet is aligned with y axis, rearrange data to fit screen
/ coordinate system for plotting.
/
IF AXIS$="Y" OR AXIS$="y" THEN
  FOR I=1 TO NUMPTS
    SWAP X(I),Y(I)
    Y(I)=-Y(I)
  NEXT I
END IF
/
/ Draw 3 plots
/
FOR I=1 TO 3
/
/ Set up graphics screen
/
  CLS
  SCREEN 9
  WINDOW (-15,11.26) - (15,-11.26)
/
/ Plot x slope errors
/
  IF I=1 THEN
    FOR J=1 TO NUMXERS
      L=IX(J) : M=JX(J)
      XCOORD=(X(L)+X(M))/2.0

```

```

YCOORD=Y(L)
IF XSLPER(J) < 0 THEN
  RAD=0.0
  WHILE RAD <= ABS(XSLPER(J))
    CIRCLE (XCOORD-26.0,YCOORD),RAD
    RAD=RAD+.05
  WEND
ELSE
  CIRCLE (XCOORD-26.0,YCOORD),ABS(XSLPER(J))
END IF
NEXT J
PRINT : PRINT "Dz/Dx Error (mrad)"
PRINT "Facet: ";ID$
PRINT USING "Rms=##.### mrad";RMSXS
PRINT "Facet too steep at unfilled points" : PRINT
PRINT USING "Scale:      =##.### mrad";XSCALE
CIRCLE (-11.5,5.5),0.75
LOCATE 1,1 : INPUT "",DUMMY$
END IF
,
Plot y slope errors
,
IF I=2 THEN
FOR J=1 TO NUMYERS
  L=IY(J) : M=JY(J)
  XCOORD=X(L)
  YCOORD=(Y(L)+Y(M))/2.0
  IF YSLPER(J) < 0.0 THEN
    RAD=0.0
    WHILE RAD <= ABS(YSLPER(J))
      CIRCLE (XCOORD-26.0,YCOORD),RAD
      RAD=RAD+.05
    WEND
  ELSE
    CIRCLE (XCOORD-26.0,YCOORD),ABS(YSLPER(J))
  END IF
NEXT J
PRINT : PRINT "Dz/Dy Error (mrad)"
PRINT "Facet: ";ID$
PRINT USING "Rms=##.### mrad";RMSYS
PRINT "Facet too steep at unfilled points" : PRINT
PRINT USING "Scale:      =##.### mrad";YSCALE
CIRCLE (-11.5,5.5),0.75
LOCATE 1,1 : INPUT "",DUMMY$
END IF
,
Plot displacement errors
,
IF I=3 THEN
FOR J=1 TO NUMPTS
  IF DISER(J) < 0.0 THEN
    RAD=0.0
    WHILE RAD <= ABS(DISER(J))
      CIRCLE (X(J)-26.0,Y(J)),RAD
      RAD=RAD+.05
    WEND
  END IF
NEXT J

```

```

ELSE
  CIRCLE (X(J)-26.0,Y(J)),ABS(DISER(J))
END IF
NEXT J
PRINT : PRINT "Displacement Error (inches)"
PRINT "Facet: ";ID$
PRINT USING "Rms=##.### inches";RMSD
PRINT "Facet too high at unfilled points" : PRINT
PRINT USING "Scale:      =##.### inch";ZSCALE
CIRCLE (-11.5,5.5),0.75
LOCATE 1,1 : INPUT "",DUMMY$
END IF
NEXT I
,
RETURN

```

References

1. Duffie, John A. and Beckman, William A., Solar Engineering of Thermal Processes, New York: John Wiley & Sons, Inc., 1979.
2. Jaffe, L. D., Optimization of Dish Solar Collectors with and without Secondary Concentrators, DOE/JPL-1060-57, Jet Propulsion Laboratory, May 1982.
3. Knasel, Don and Ehresman, Derik, Solar Concentrator Advanced Development Program Final Report, NASA CR-185173, Harris Corporation.
4. McClure, Donald J., Design & Demonstration of a System for the Deposition of Atomic-Oxygen Durable Coatings for Reflective Solar Dynamic Power System Concentrators, NASA Contractor Report 4158, 3M Corporation, 1988.
5. Twiddle, British J. of Applied Physics, Vol. 8, Aug. 1957, p. 338, as reported by Sunflower Solar Collector, NASA CR-46, Thompson Ramo Wooldridge, Inc., May 1964.
6. COSMOS/M, Version 1.61, Structural Research and Analysis Co., CA.
7. Press, William H., Flannery, Brian P., Teukolsky, Saul A., and Vetterling, William T., Numerical Recipes, New York: Cambridge University Press, 1986.

**Table 2.1
Metal Candidates and Properties**

	Density (lbs/in ³)	Tensile Modulus (psi)	Coeff. of Thermal Expansion (°F ⁻¹)	Thermal Conductivity Btu (hr. ft ² °F/ft) ⁻¹	Relative Face Sheet Thickness	Relative Face Sheet Mass	Relative Thermal Distortion
Aluminum	0.097	10.5E6	13E-6	80	1	1	1
Titanium	0.16	15.5E6	5.5E-6	11	0.88	1.4	4.9
Stainless Steel	0.29	29E6	9E-6	9	0.71	2.1	18
Beryllium	0.0668	42E6	7E-6	90	0.63	0.42	0.3
Magnesium	0.0628	6.5E6	14.5E-6	45	1.17	0.80	1.3

Table 3.1
Material Properties of Thermal Analysis

MATERIAL	THERMAL CONDUCTIVITY (W/mil/°K)	THERMAL CONDUCTIVITY (J/min-mil/°K)	DENSITY (LB/MIL³)	HEAT CAPACITY (J/LB/°K)
TOP-SKIN	5.08E-03	0.305	9.8E-11	395
BOTTOM-SKIN	5.08E-03	0.305	9.8E-11	395
HONEYCOMB	5.08E-03	0.305	9.8E-11	395
EPOXY-I	5.10E-05	3.06E-03	4.0E-11	854
EPOXY-II	5.10E-05	3.06E-03	4.0E-11	854

PARAMETERS OF THE RADIATION HEAT TRANSFER

SURFACE	ABSORBSIVITY	EMISSIVITY
TOP-SKIN	0.12	0.5
BOTTOM-SKIN	0.20	0.12

INITIAL TEMPERATURE 300 °K
 BOLTZMAN CONSTANT 2.195E-15 J/min/mil/°K⁴

Table 5.1
Properties of Levelling and Reflective Coats

	<u>Levelling Coat</u>	<u>Aluminum</u>
Thickness	$3 \times 10^{-6} \text{m}$	800 °A
Density	1.45 gm/cm ³	0.09 lbm/in ³
Thermal Conductivity (Btu/ft.-hr.-°F)	0.847	144
Specific Heat	0.26 cal/mg-°C	0.224 Btu/lbm-°F
Young's Modulus	400,000 psi	10.7×10^6 psi
Shear Modulus	4,000,000 psi at 77 °F	----
Moisture Absorptance	3-4% wt.	----
Tensile Strength	19,000 psi	6,000 psi

Table 8.1
Sensitivity of Measured Local Slope Error to Direction of Scan

<u>Scan Direction</u>	<u>Slope Error (mrad)</u>		
	<u>X</u>	<u>Y</u>	<u>Combined</u>
X	.35	.35	.49
Y	.32	.41	.52

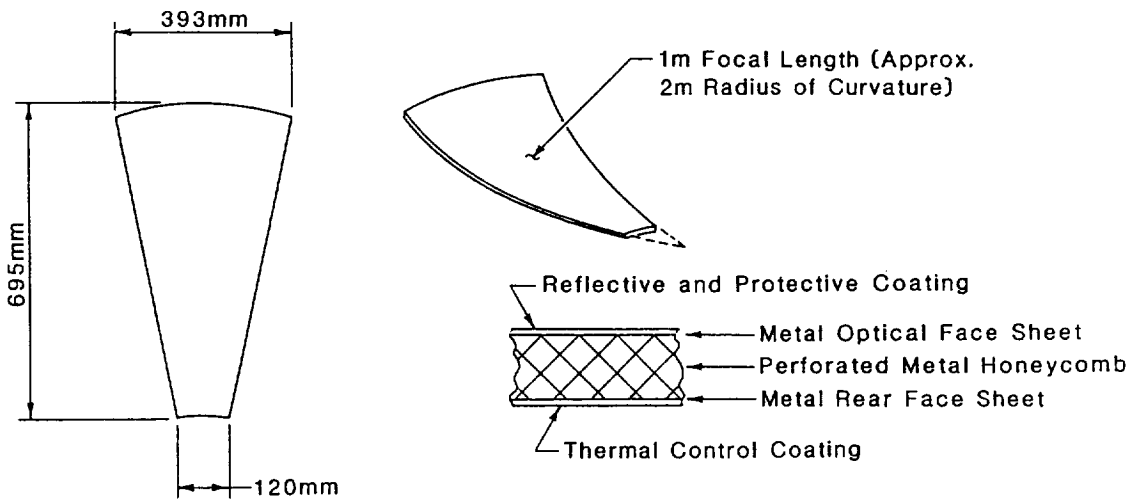


Figure 1.1 Facet Configuration.

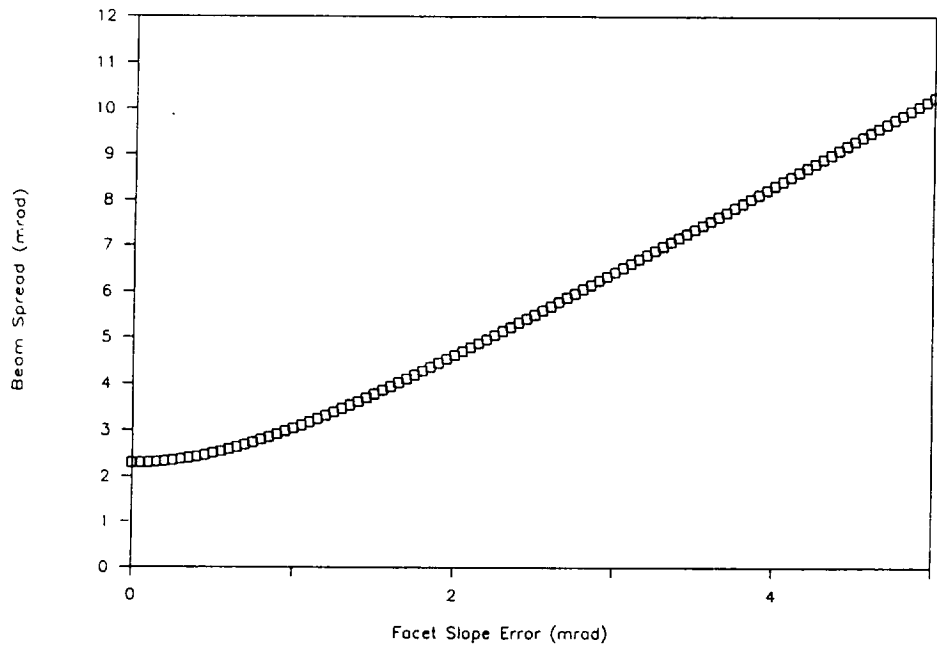


Figure 2.1 Relative Sensitivity to Slope Error.

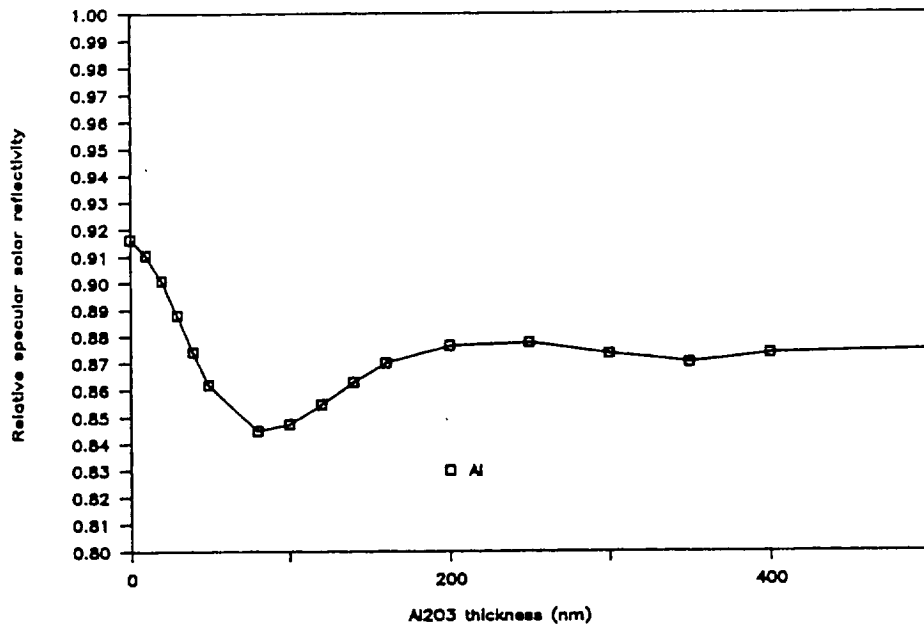


Figure 2.2 Calculated Reflectance Spectra Averaged over AMO for Al as a Function of Al₂O₃ Overcoat Thickness. (Ref.4)

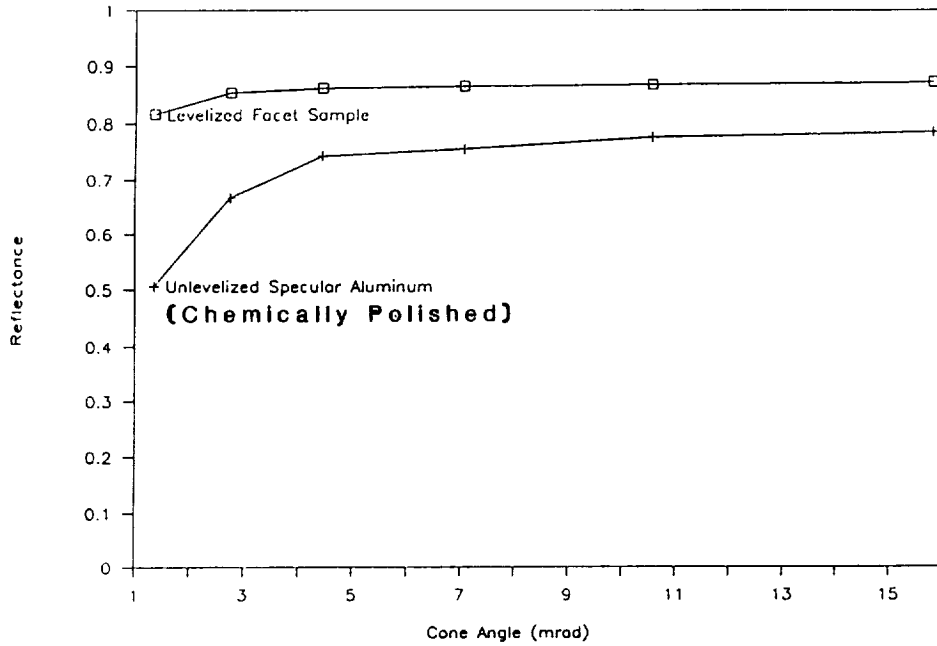


Figure 2.3 Reflectance of Specular Aluminum.

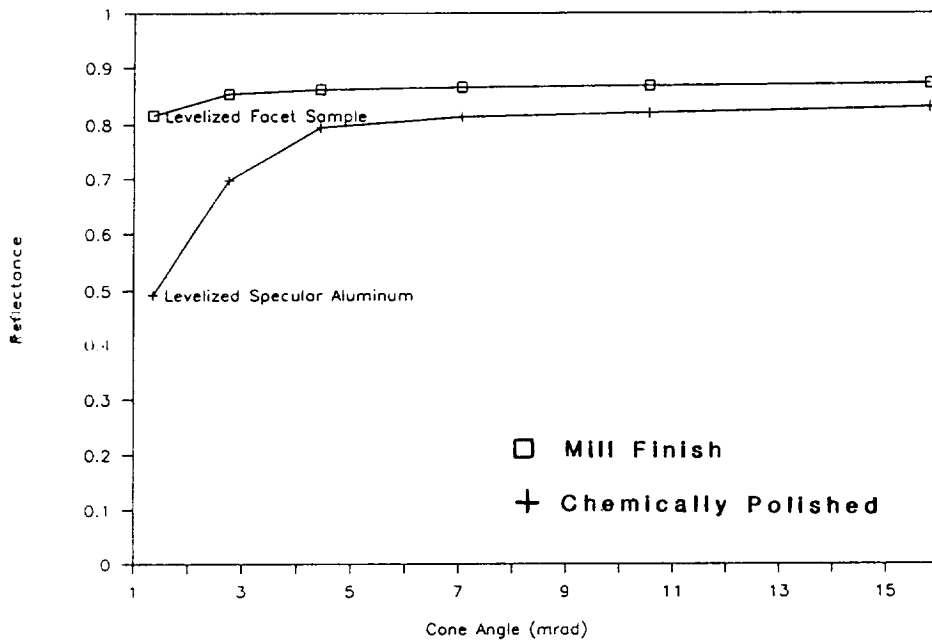


Figure 2.4 Reflectance of Levelized Aluminums.



Figure 2.5 Soldered Facet Sample.

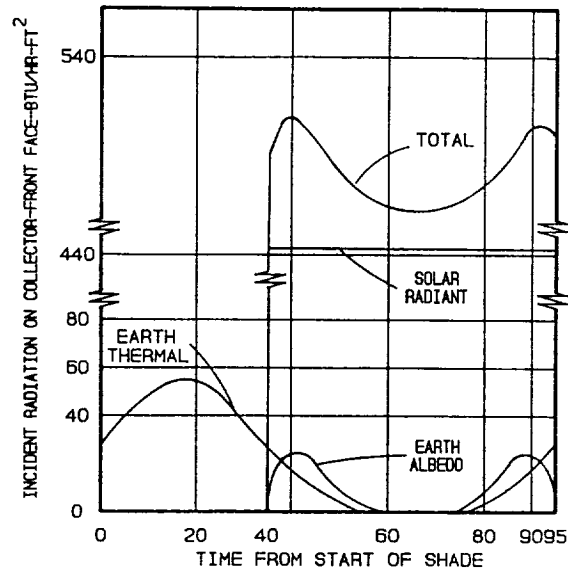


Figure 3.1 Incident Radiation on Front Face of Concentrator

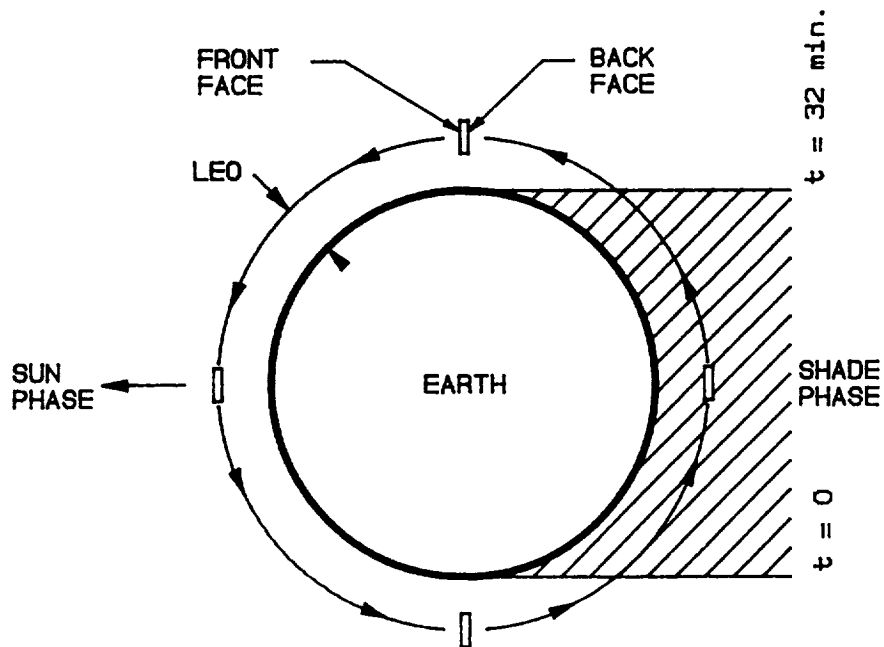
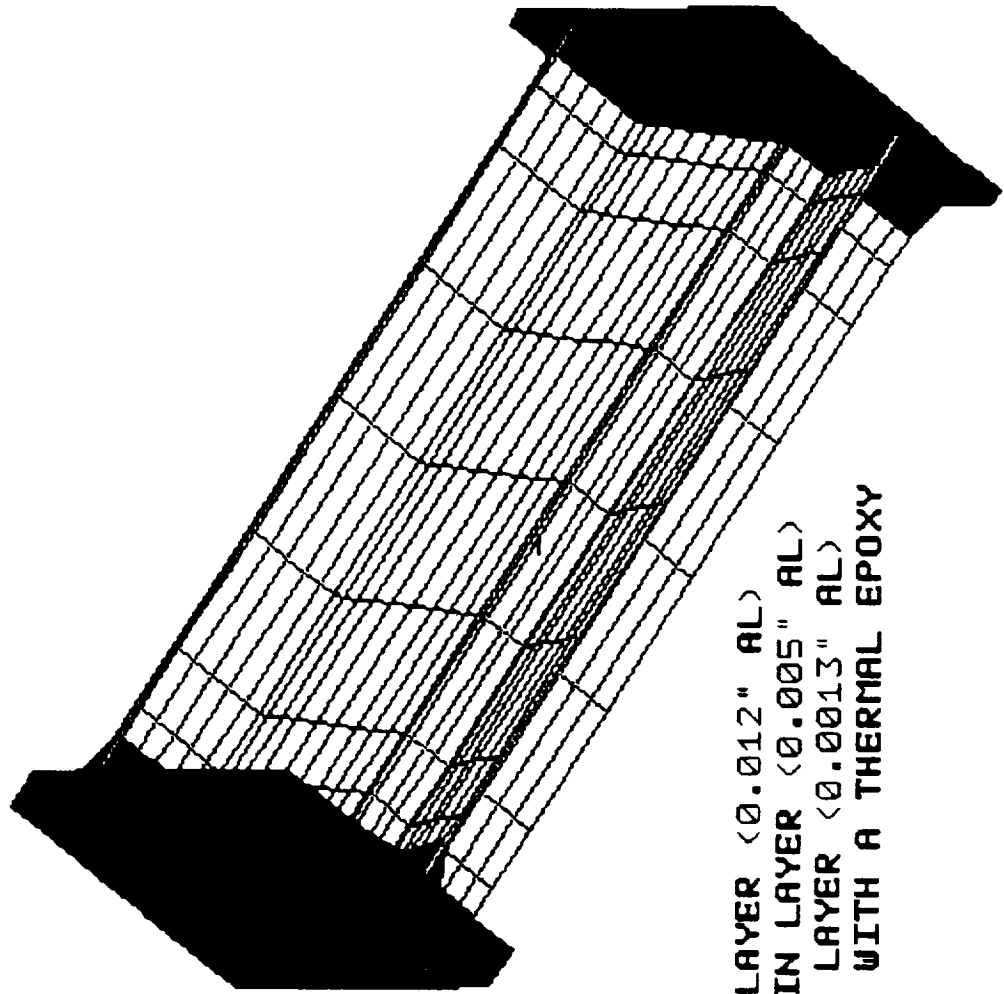


Figure 3.2 Orbit Geometry for the Collector

Figure 3.3 Finite Element Model of Unit Cell



TOP SKIN LAYER <0.012" AL>
BOTTOM SKIN LAYER <0.005" AL>
HONEYCOMB LAYER <0.0013" AL>
ASSEMBLED WITH A THERMAL EPOXY



Figure 3.4 Transient Temperature Response of the Facet

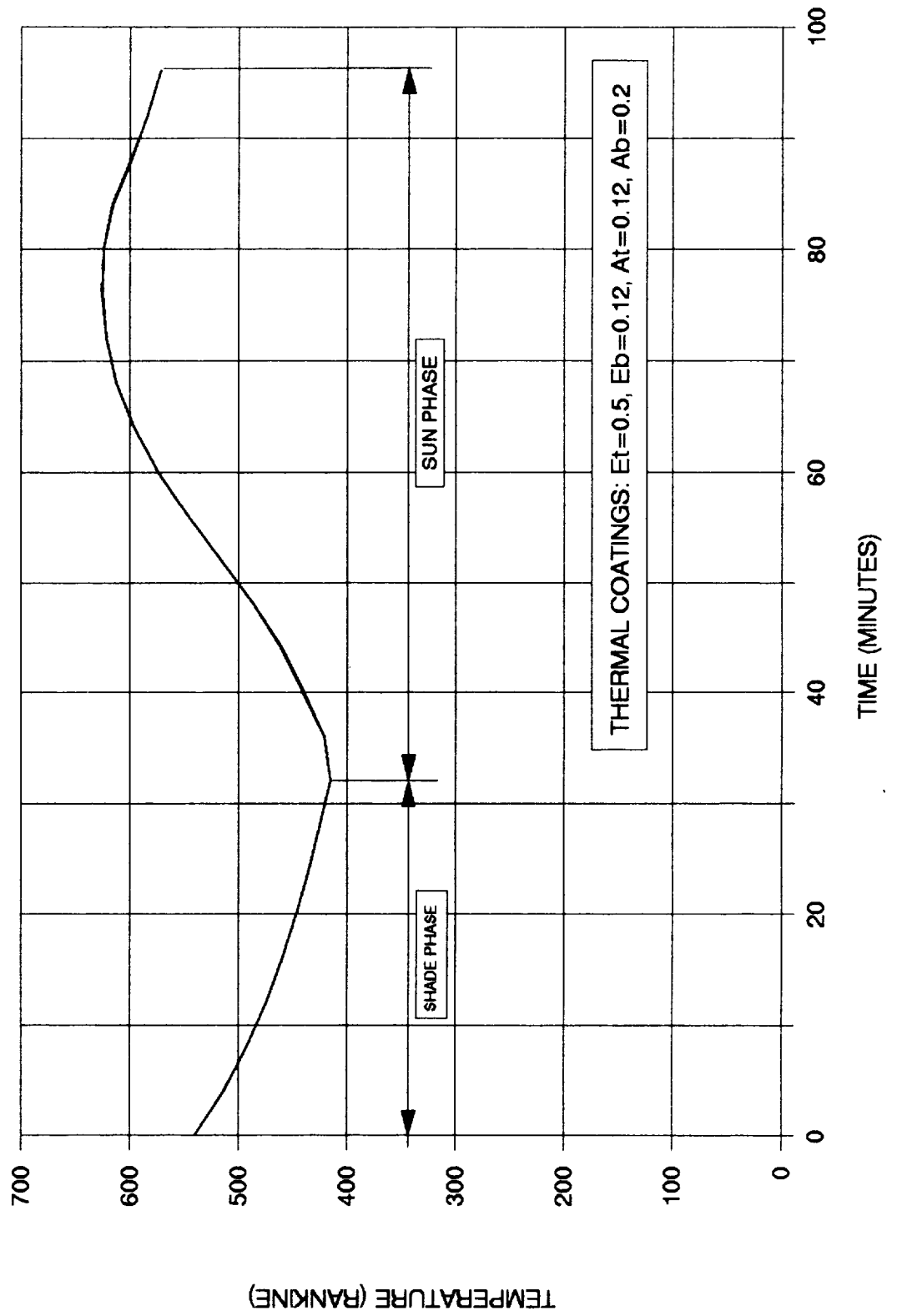


Figure 3.5 Contour Plot of Facet Displacement at Low Temperature

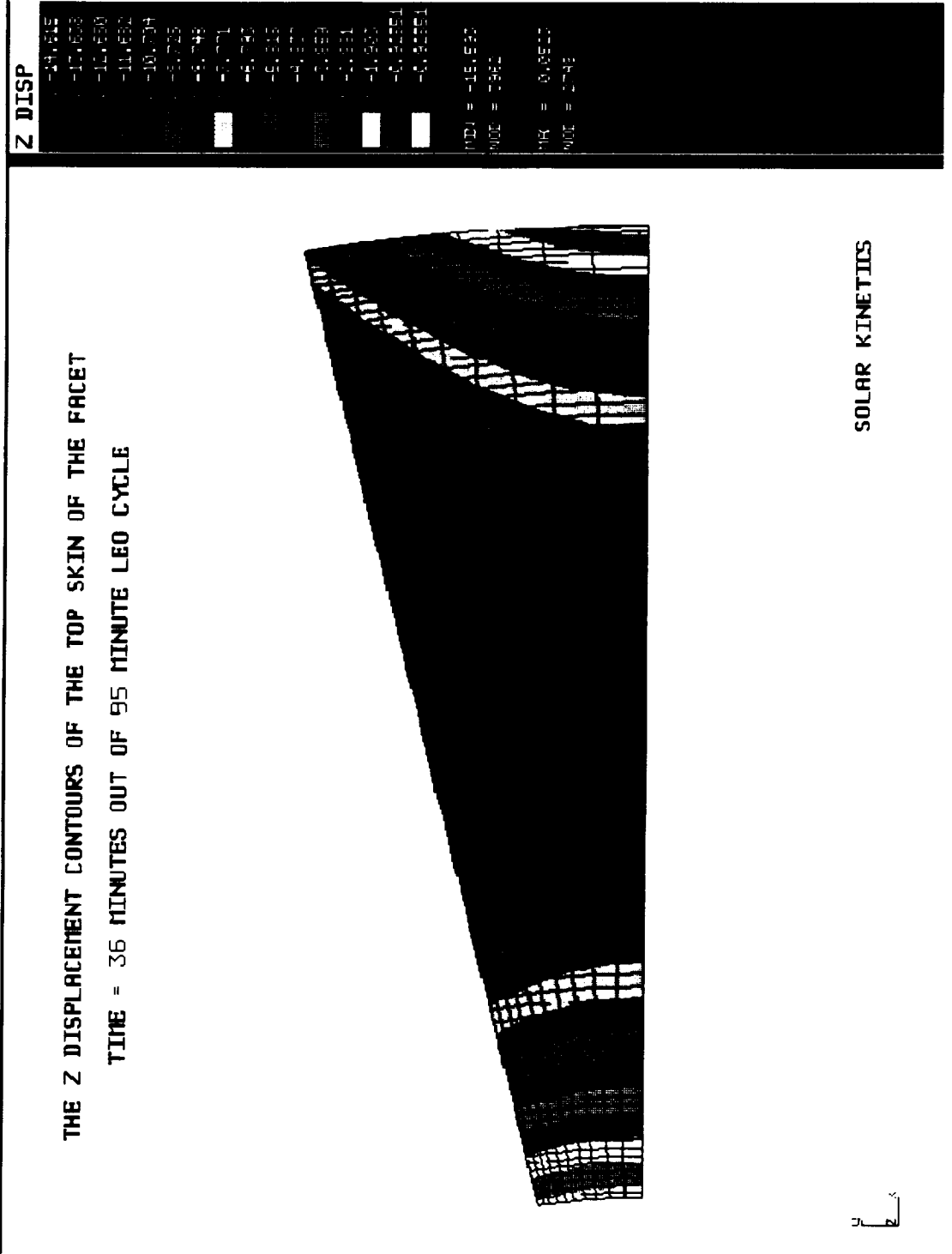
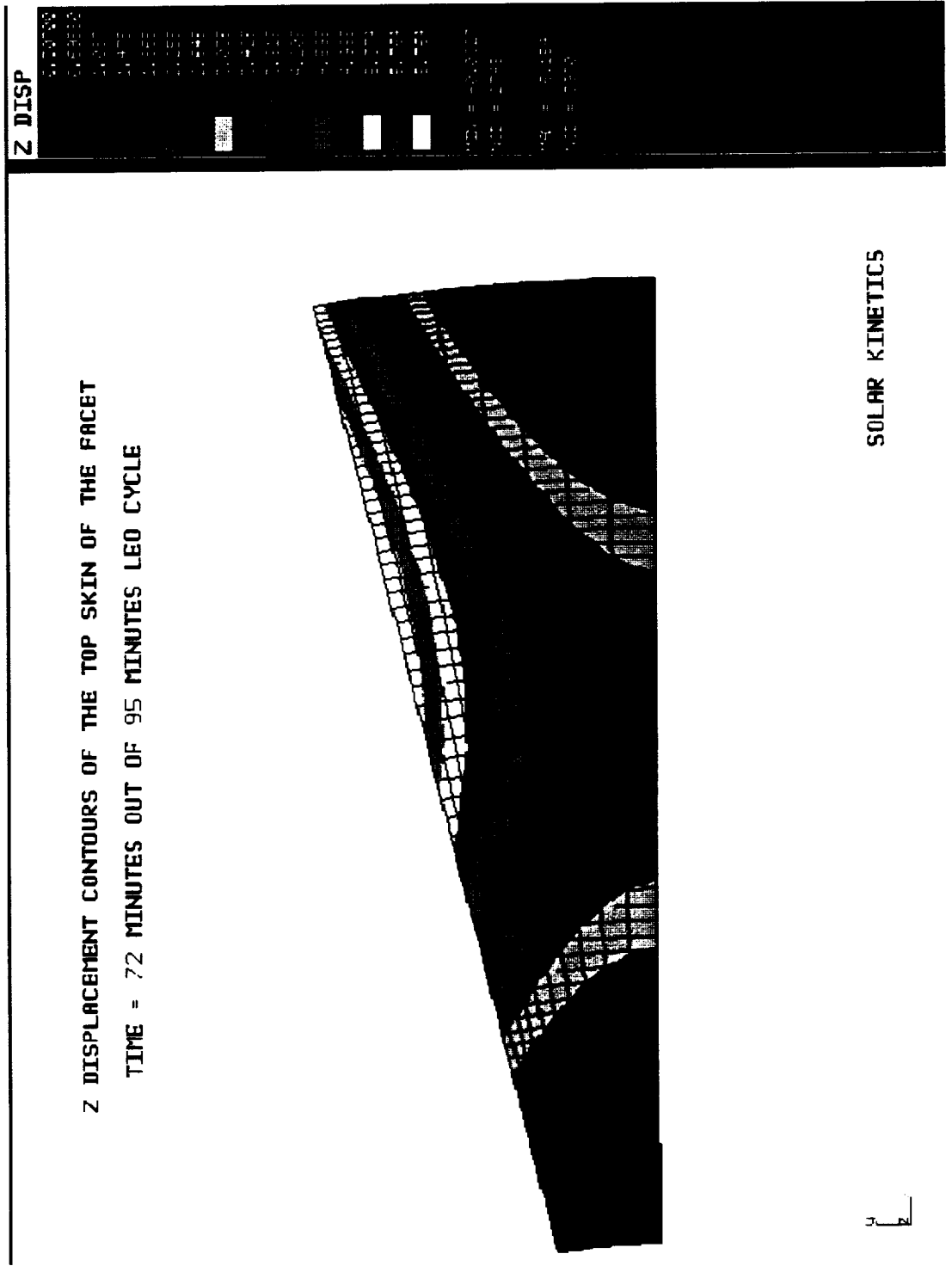


Figure 3.6 Contour Plot of Facet Displacement at High Temperature



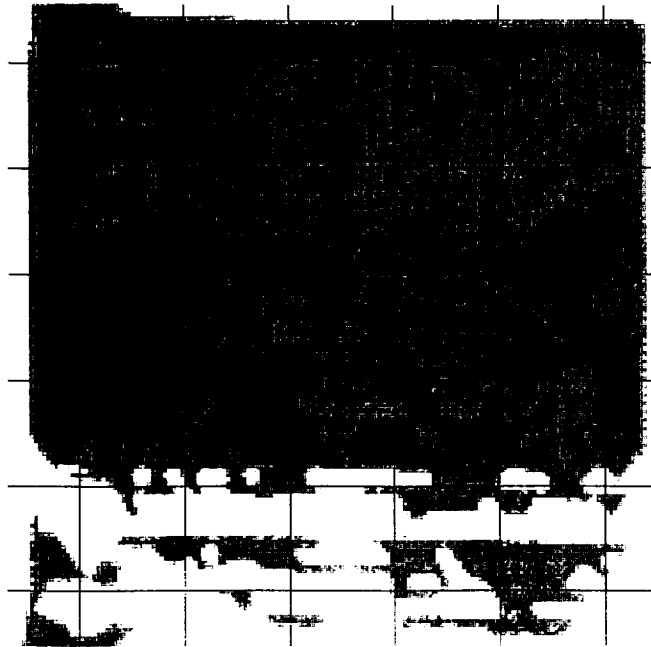


Figure 4.1 Ultrasonic Results of Early Facet Sample.

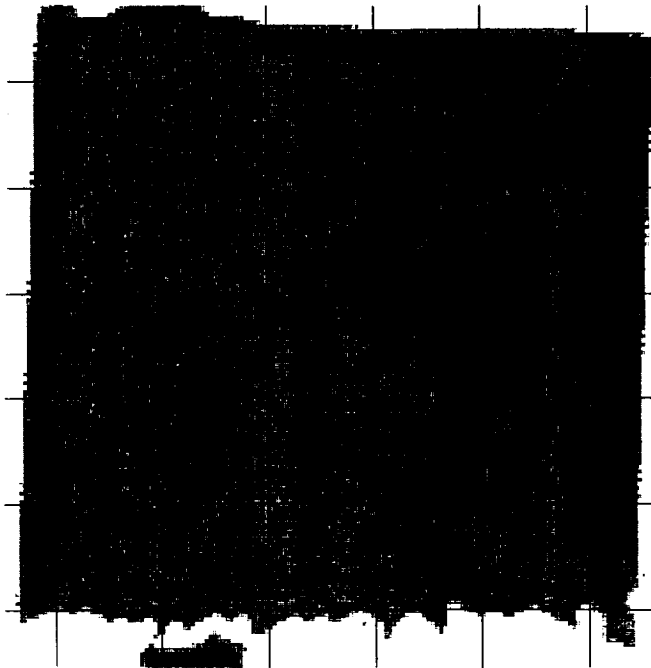


Figure 4.2 Ultrasonic Results of Later Facet Sample.

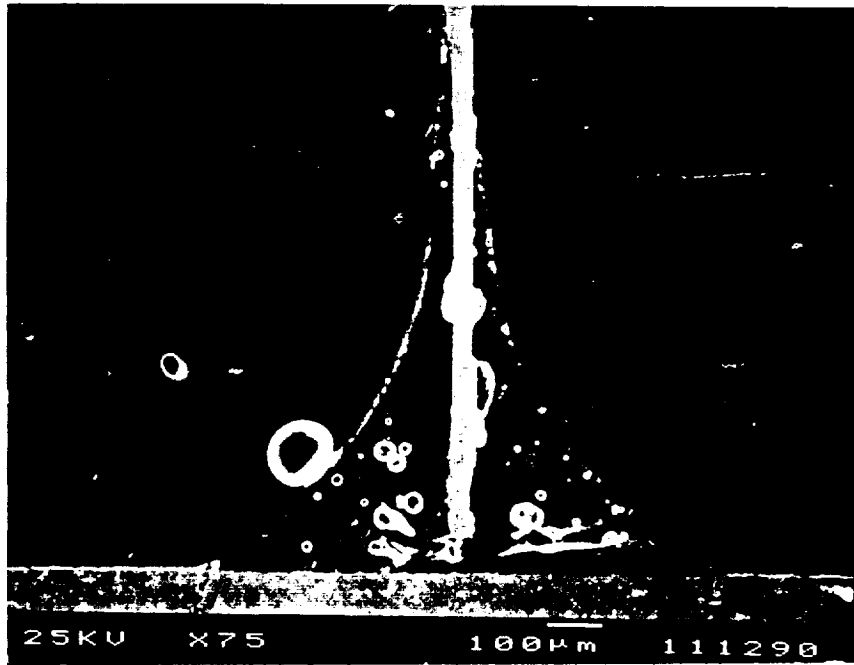


Figure 4.3 Microscopic View of Adhesive Cross Section.

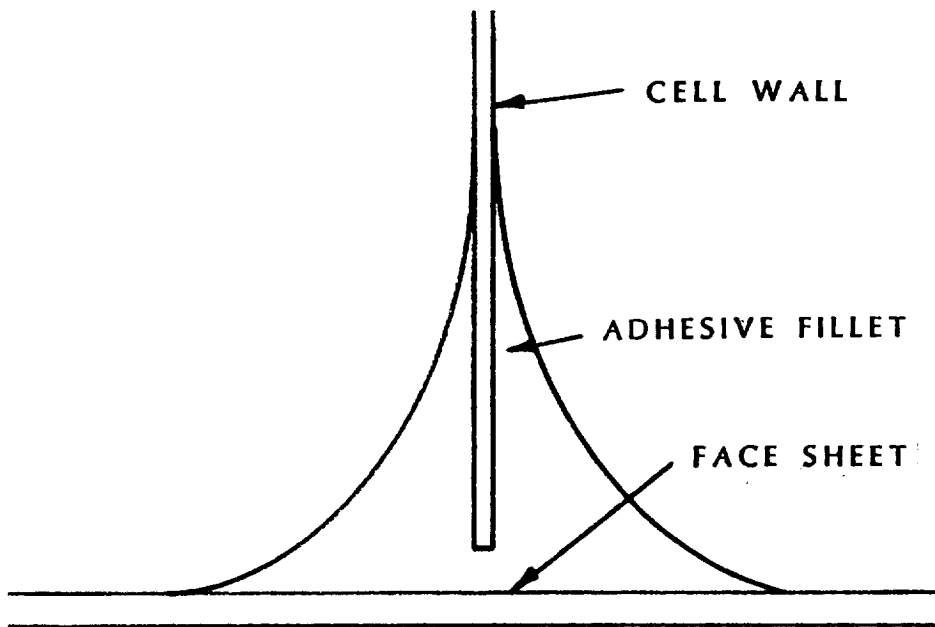


Figure 4.4 Descriptive Outline of Adhesive Cross Section.

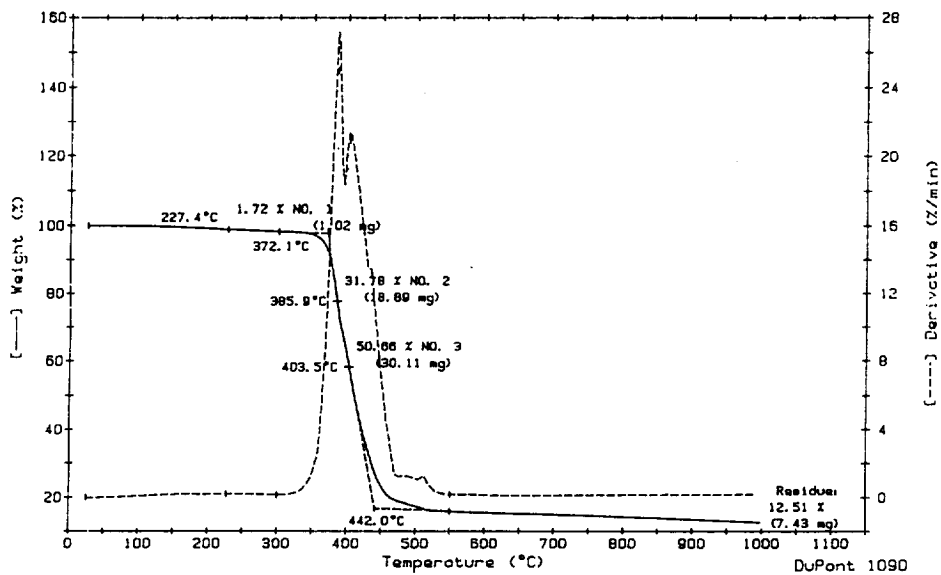


Figure 5.1 Thermal Gravimetric Analysis of Polyimide Material.

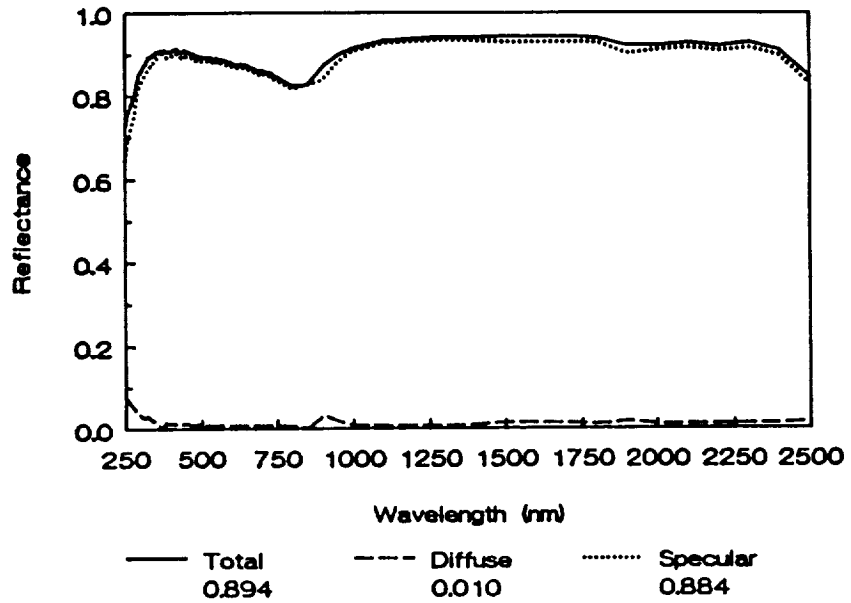


Figure 5.2.a Specular Reflectance of Fully Coated Sample for 250-2500 nm Wavelength (Perkin Elmer Lambda-9 Data).

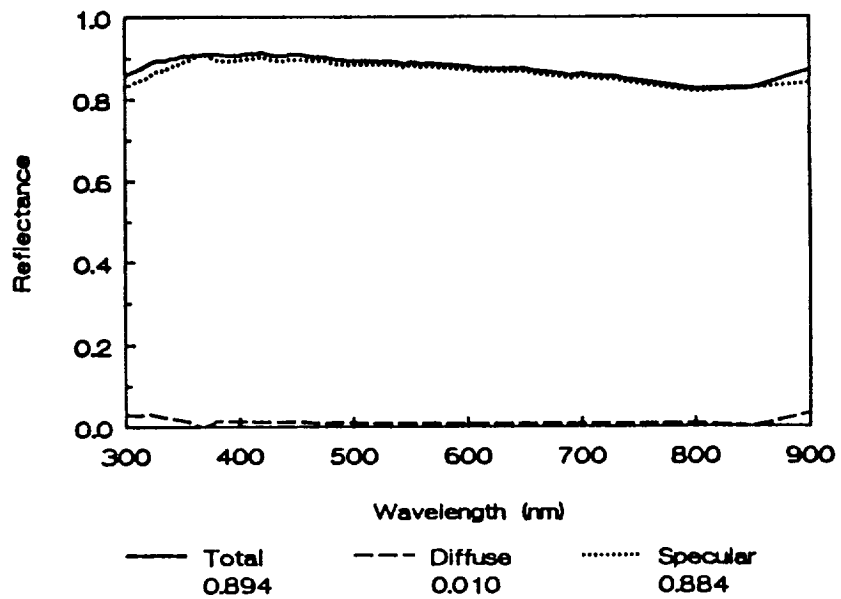


Figure 5.2.b Specular Reflectance of Fully Coated Sample for 300-900 nm Wavelength (Perkin Elmer Lambda-9 Data).

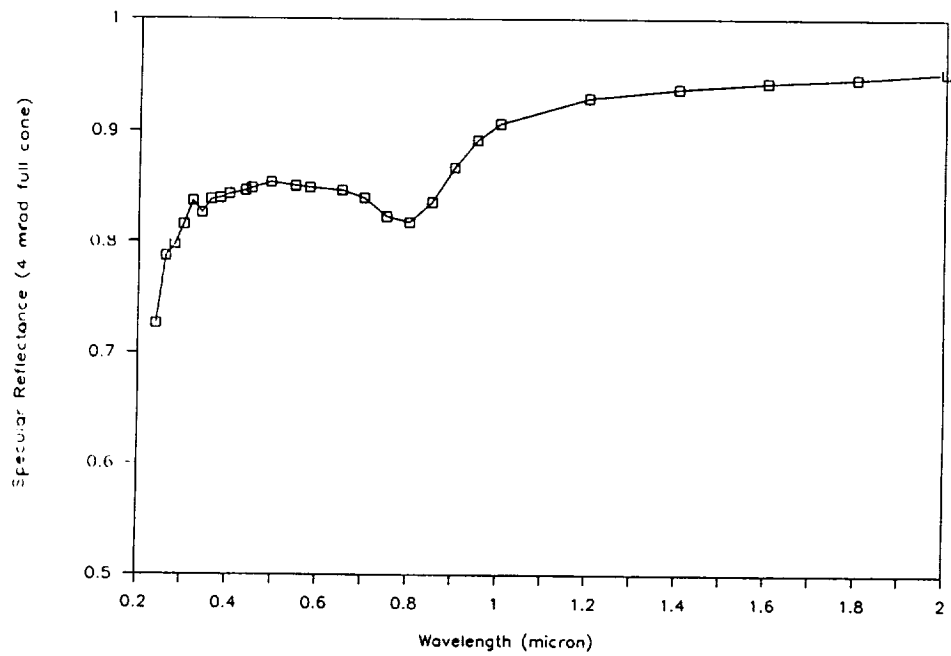


Figure 5.2.c Specular Reflectance of Coated Sample.

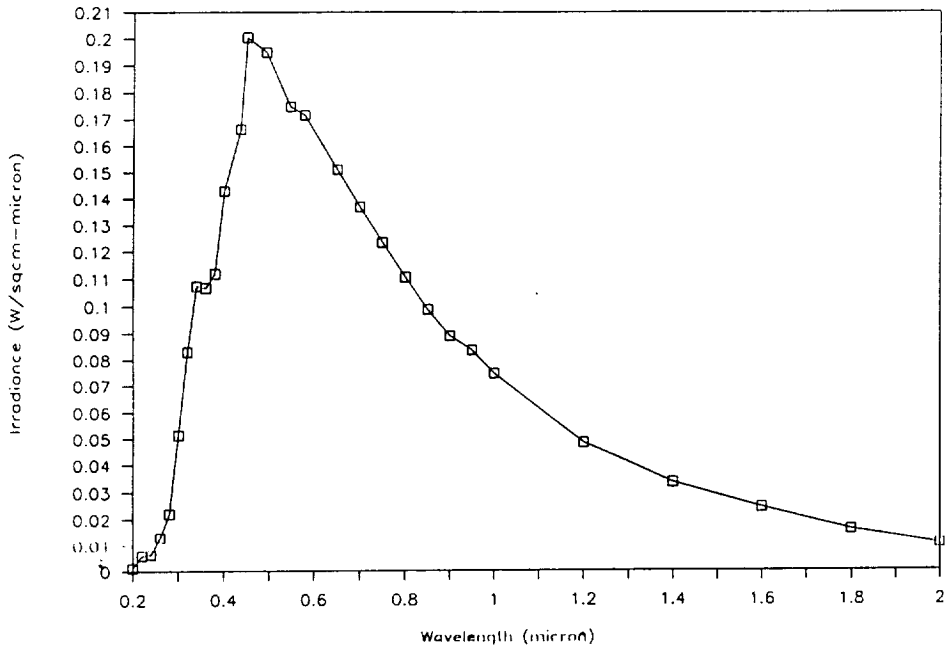


Figure 5.3 Distribution of Extraterrestrial Solar Radiation.

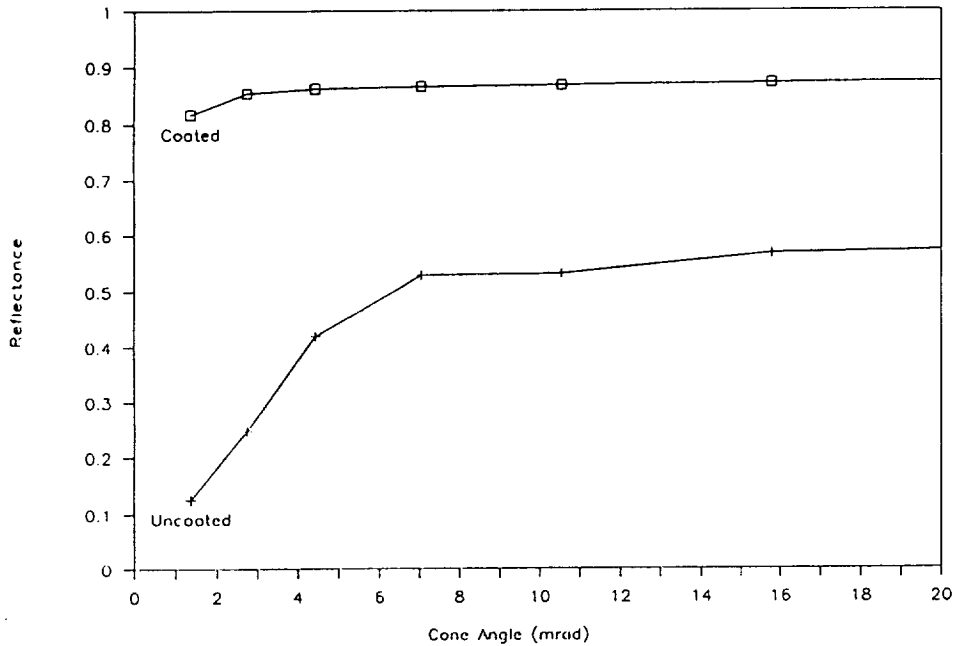


Figure 5.4 Reflectivity vs. Cone Angle for Coated and Uncoated Samples of Mill Finished Aluminum (at 633 nm).

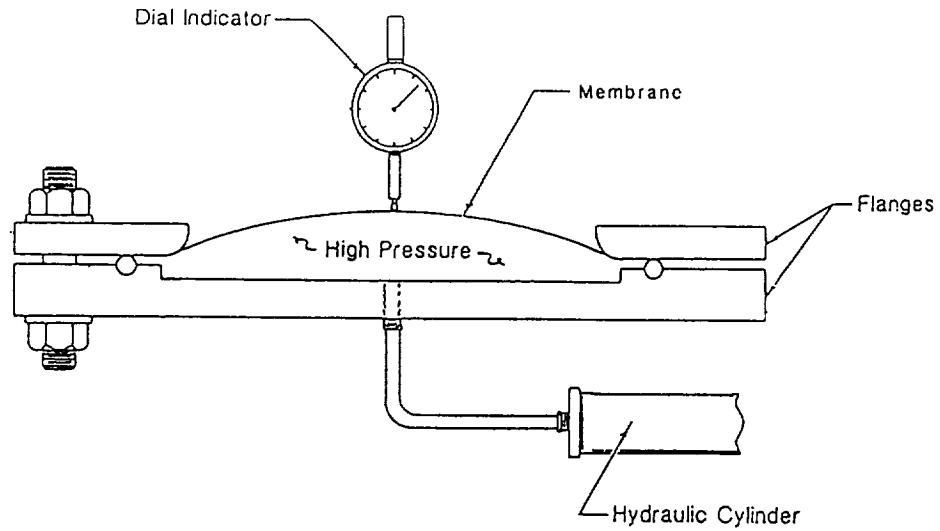


Figure 6.1 Schematic Description of Sheet-Forming Apparatus.

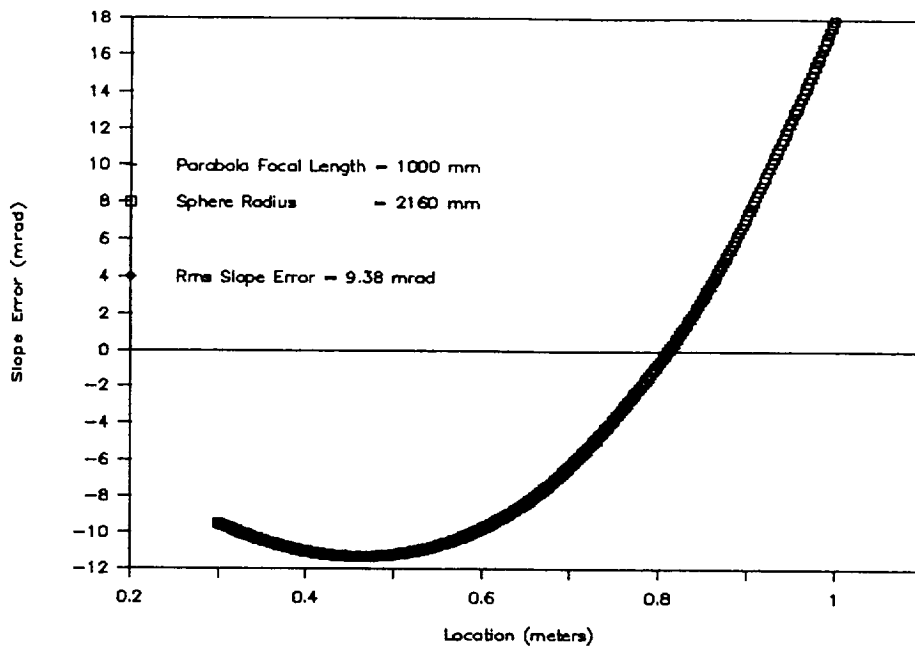


Figure 6.2 Relative Difference of Sphere and Parabola.



Figure 7.1 Mold and Air Filtering Equipment.

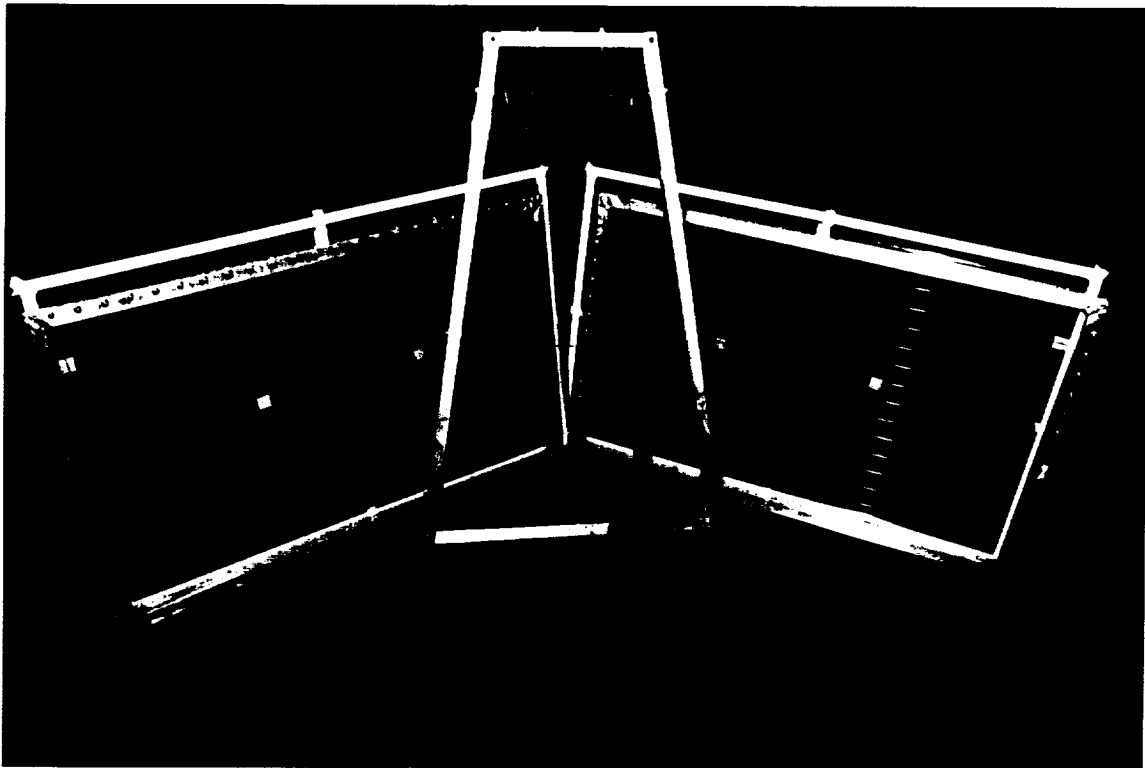


Figure 7.2 Tooling used for Adhesive Application and Core Transfer.

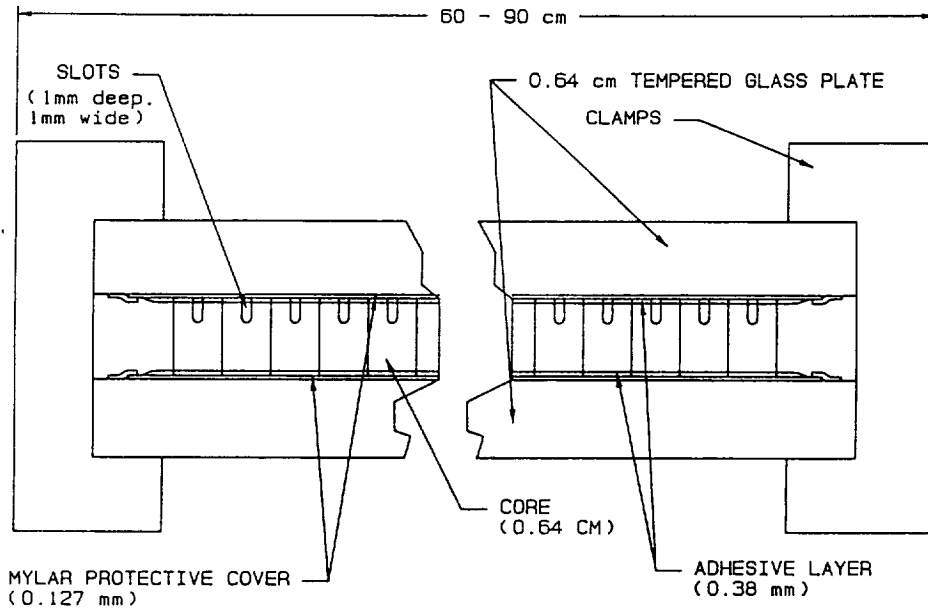


Figure 7.3 Application of Adhesive to Core.

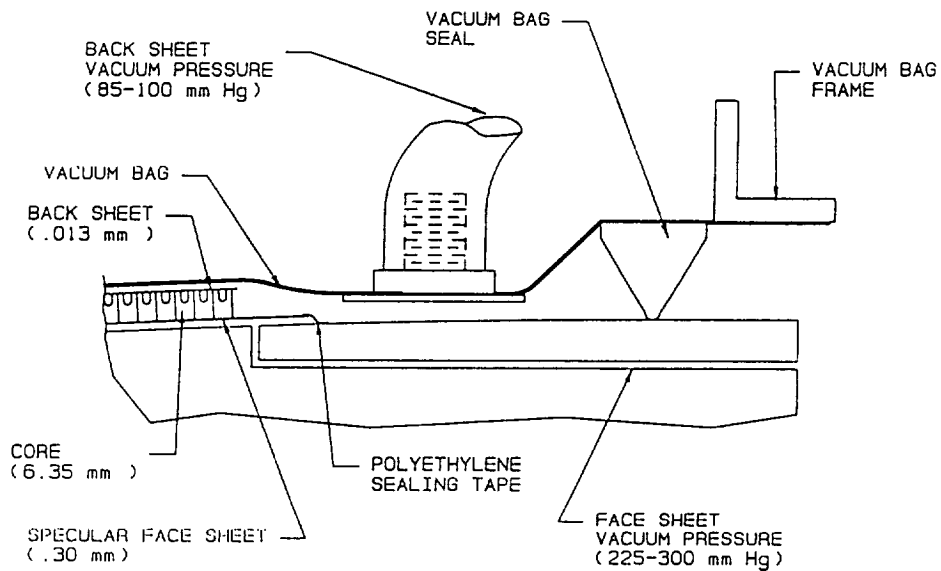


Figure 7.4 Cross Section of Facet on Mold with Vacuum Bag.

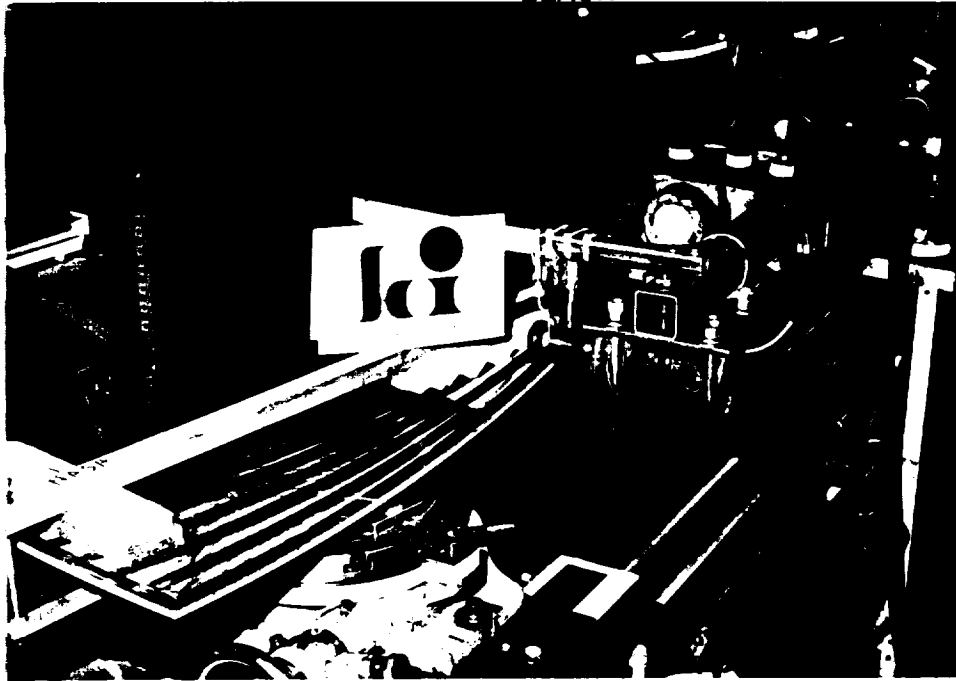


Figure 7.5 Panel Saw Apparatus.

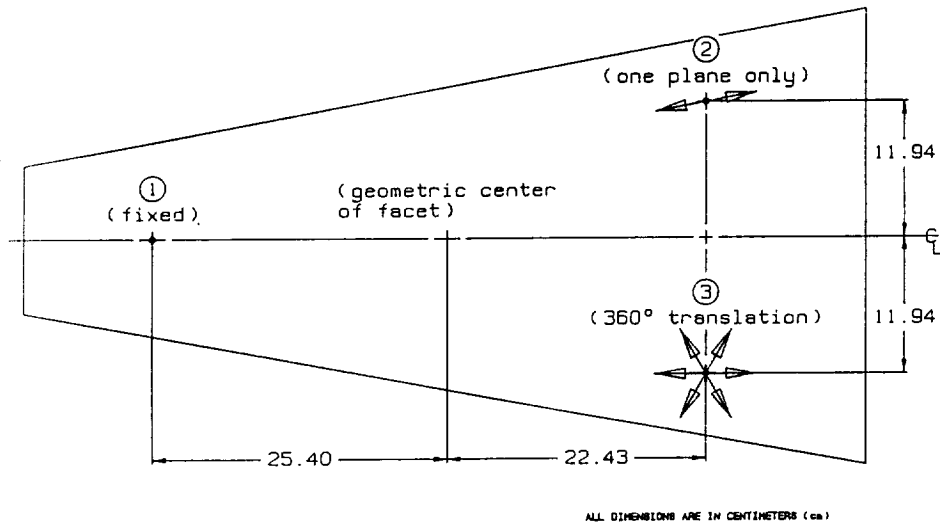


Figure 7.6 Location and Degrees of Freedom of Mounting Hardware.

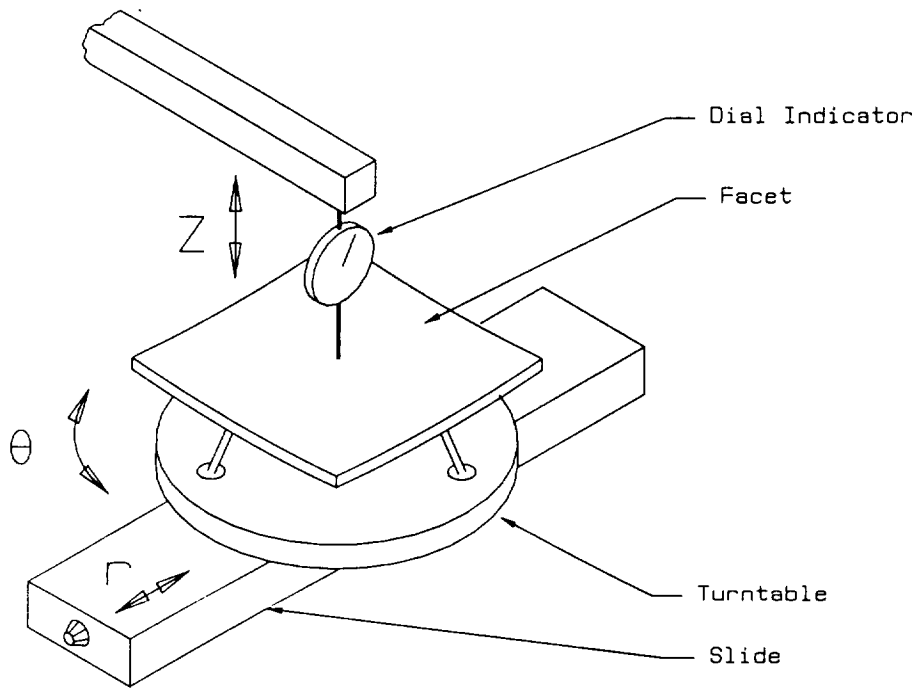


Figure 8.1 Means of Measuring Contour of 300 mm Facet Samples.

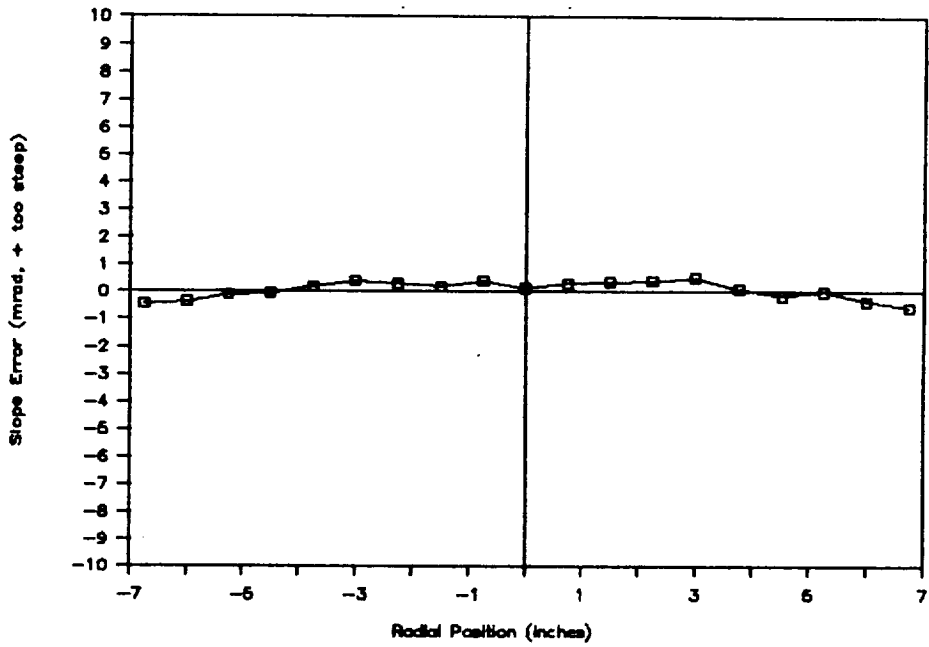


Figure 8.2 Typical Contour Results for a 300 mm Facet Sample.

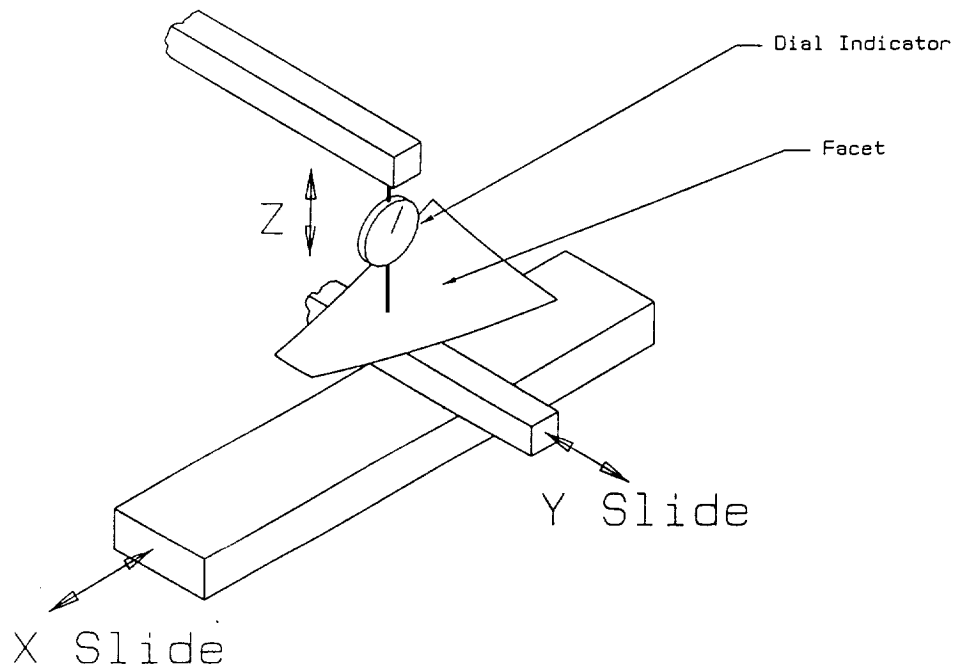


Figure 8.3 Means of Measuring Contour of Full-Sized Facets.



Figure 8.4 Equipment Used for Some Contour Measurements of Full-Sized Facets.

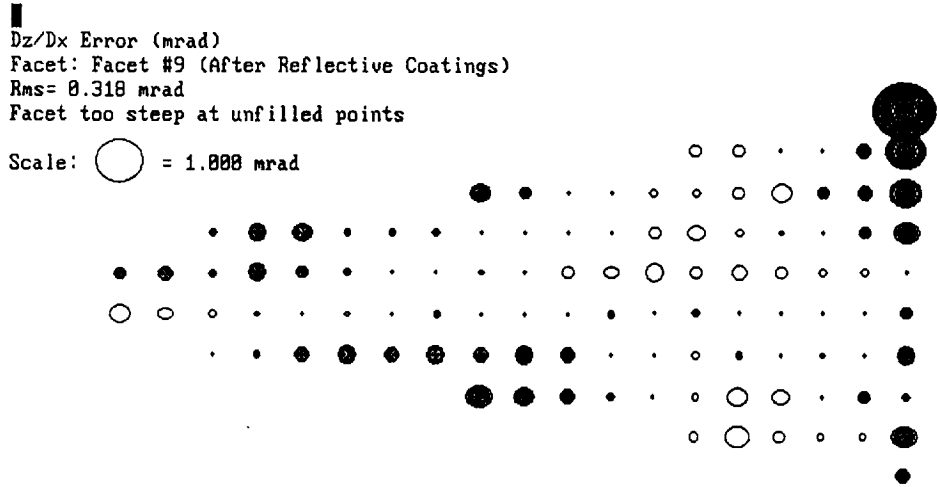


Figure 8.5 Slope Error (About Y Axis) of Full-Sized Facet.

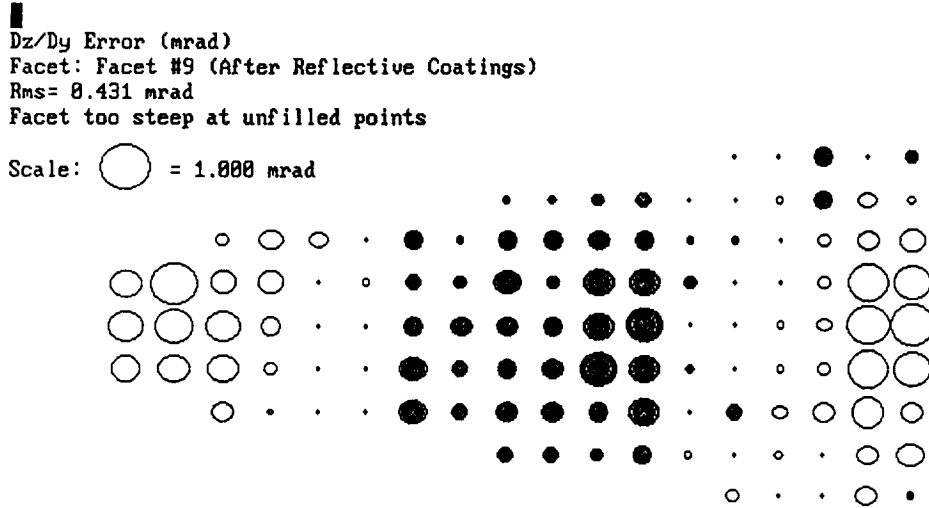


Figure 8.6 Slope Error (About X Axis) of Full-Sized Facet.

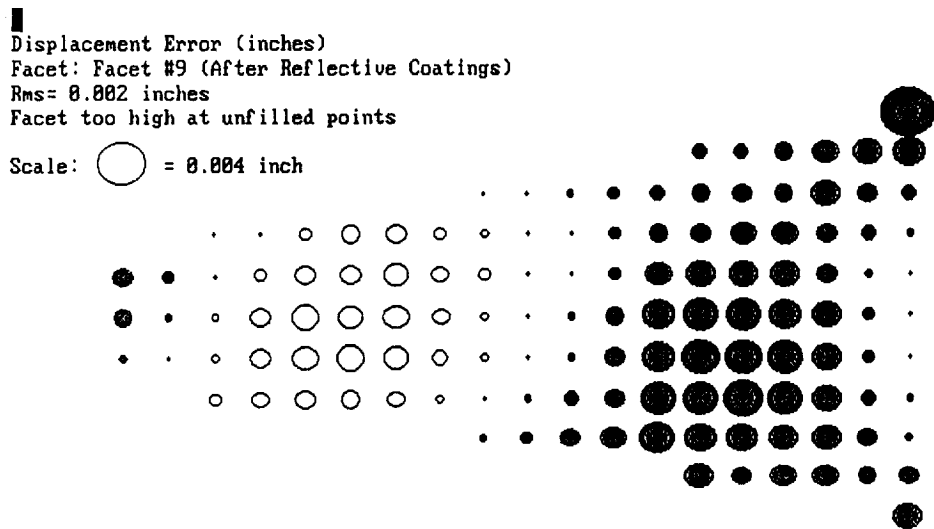


Figure 8.7 Displacement Error of Full-Sized Facet.

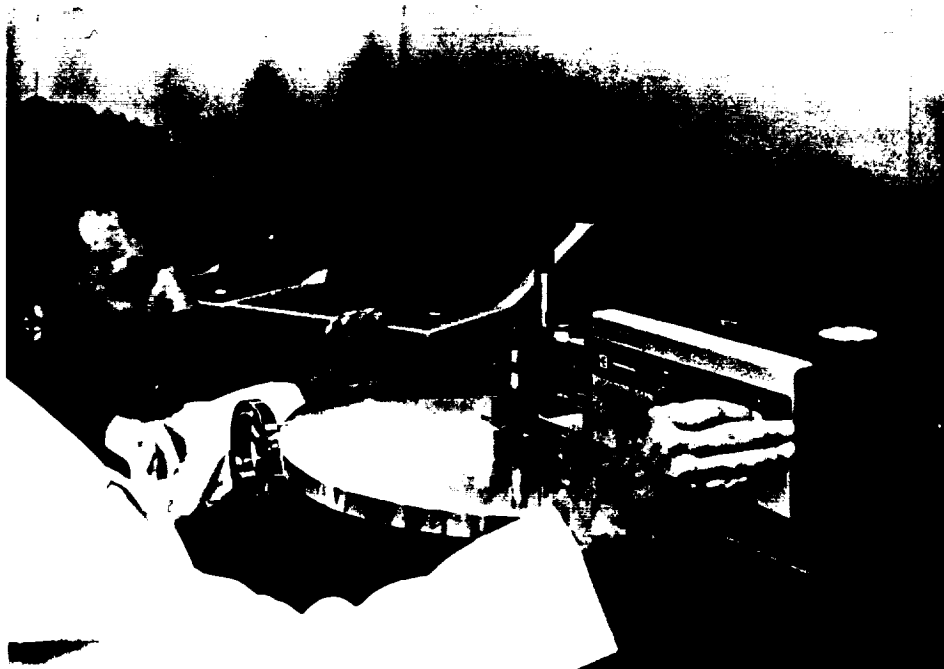


Figure 8.8 Surface Analyzer Used to Measure Local Slope Error of Uncoated Facets.

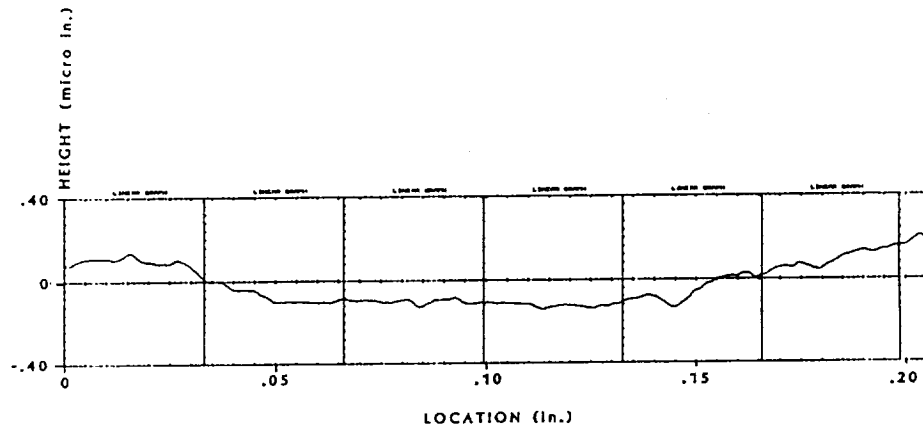


Figure 8.9 Typical Results from Surface Analyzer.

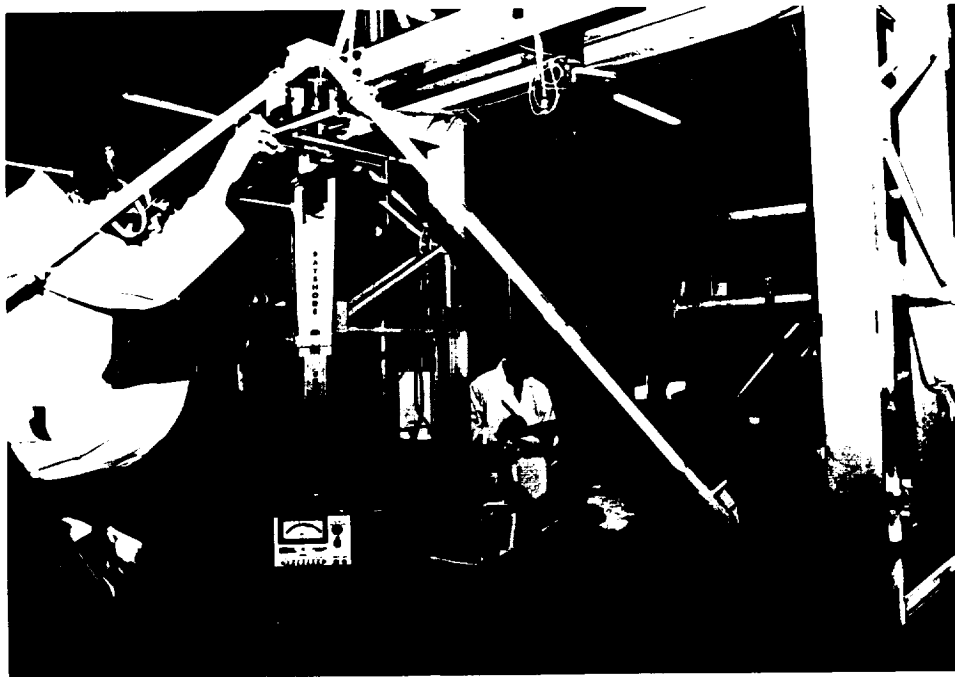


Figure 8.10 Testing of a Full-Size Facet With the Laser Measurement System.

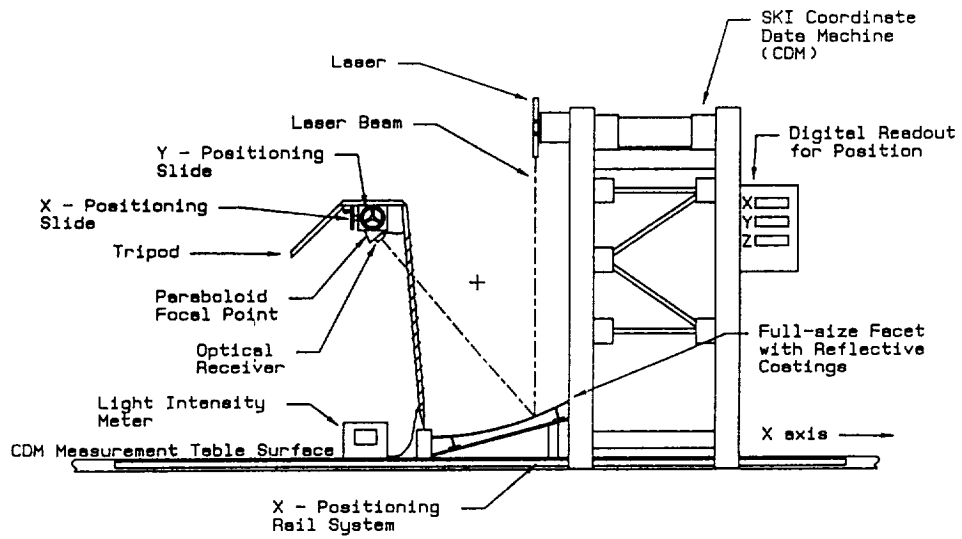


Figure 8.11 Laser Measurement System Description.

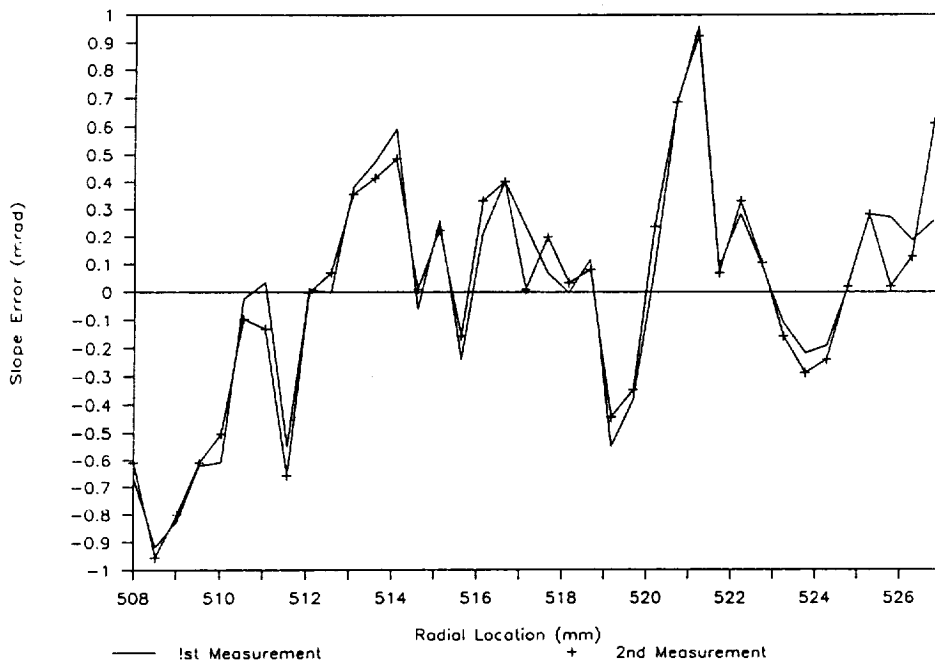


Figure 8.12 Repeatability Tests of Laser Measurement for Surface Dimpling.




Figure 9.1 Assembled Facet with all Coatings Mounted in a Display Case.

ORIGINAL PAGE
BLACK AND WHITE PHOTOGRAPH

ORIGINAL PAGE IS
OF POOR QUALITY

CLASSIFICATION

		Report Documentation Page	
1 Report No. NASA CR- 189109	2. Government Accession No.	3. Recipient's Catalog No.	
4. Title and Subtitle Development of an Improved Mirror Facet for Space Applications		5. Report Date October 91	6. Performing Organization Code
		8. Performing Organization Report No. None	
7 Author(s) Paul Schertz, Shabbar Saifee, and Luke Lammert		10. Work Unit No.	
		11. Contract or Grant No. NAS3-25632	
9. Performing Organization Name and Address Solar Kinetics, Inc. 10635 King William Dr. Dallas, TX 75220		13. Type of Report and Period Covered Contractor Report Final	
		14. Sponsoring Agency Code	
12. Sponsoring Agency Name and Address National Aeronautics and Space Administration Lewis Research Center Cleveland, Ohio 44135-3191			
15. Supplementary Notes Final Report. Project Manager, Ted Mroz, NASA Lewis.			
16. Abstract <p>A fabrication technique was successfully developed for a metallic aluminum honeycomb, high-accuracy, lightweight, and long-life solar concentrator (mirror) for Advanced Solar Dynamic Space Power Systems. The program scope was limited to the development, fabrication, evaluation, and delivery of a solar concentrator facet (petal) that was sized for a 2-meter diameter deployable solar concentrator. A surface accuracy of 1.0 mrad was achieved. The development incorporated tooling design, material selection, facet forming, adhesive selection, testing, and analysis. Techniques for applying levelizing, reflective, and protective optical coatings were also developed.</p>			
17. Key Words (Suggested by Author(s)) Solar Dynamic, Concentrator, Mirror, Reflector		18. Distribution Statement	
19. Security Classif. (of this report) Unclassified	20. Security Classif. (of this page) Unclassified	21. No of pages	22. Price*
<p style="text-align: center;">"NATIONAL SECURITY INFORMATION"</p> <p style="text-align: center;">Unauthorized Disclosure Subject to Criminal Sanctions.</p>		CLASSIFIED BY: _____	
		DECLASSIFY ON: _____	
WHEN SEPARATED FROM ENCLOSURES, HANDLE THIS DOCUMENTATION PAGE AS: _____			

CLASSIFICATION